








RESEARCH ARTICLE

10.1029/2022JD038196

Wet and Dry Cold Surges Over the Maritime Continent

I. Tan¹ , M. J. Reeder^{1,2} , M. S. Singh^{1,2} , C. E. Birch³ , and S. C. Peatman³ 

Special Section:

Years of the Maritime Continent

¹School of Earth, Atmosphere and Environment, Monash University, Clayton, VIC, Australia, ²Australian Research Council Centre for Climate Extremes, Clayton, VIC, Australia, ³Institute of Climate and Atmospheric Science, School of Earth and Environment, University of Leeds, Leeds, UK

Key Points:

- Cold surges occur on approximately 18% of days over a 20-year analysis period, and account for approximately 30% of the total rainfall
- Locally, wet cold surges are characterized by a moister free troposphere, which allows convection to penetrate the lower troposphere
- Regionally, dry (wet) surges usually form in the suppressed (active) Madden-Julian Oscillation phases and are sometimes linked to the Australian summer monsoon

Correspondence to:

I. Tan,
isaac.tan@monash.edu

Citation:

Tan, I., Reeder, M. J., Singh, M. S., Birch, C. E., & Peatman, S. C. (2023). Wet and dry cold surges over the Maritime Continent. *Journal of Geophysical Research: Atmospheres*, 128, e2022JD038196. <https://doi.org/10.1029/2022JD038196>

Received 27 NOV 2022
Accepted 6 JUN 2023

Abstract Cold surges are synoptic weather systems that occur over the Maritime Continent during the boreal winter. They are characterized by the strengthening of prevailing low-level northerly to north-easterly winds, temperature falls of a few degrees over several days, and in some cases, heavy prolonged rainfall and flooding. We investigate the synoptic structure and development of cold surges through composites of dry, moderate and wet surges. Each surge category is defined by the distribution of precipitation averaged within a specified domain over the equatorial South China Sea. Dry surges are characterized by cross-equatorial flow and positive mean sea-level pressure anomalies that reach the Southern Hemisphere, and enhanced descent or weaker ascent. Wet surges are characterized by limited cross-equatorial flow, low-pressure anomalies over the equator, and enhanced moisture and ascent. The local diurnal precipitation patterns are consistent with the convection being controlled by the mid-tropospheric buoyancy of an idealized entraining plume. This buoyancy diagnostic suggests that wet surges are characterized by a moister free troposphere because this reduces the effect of entrainment and allows deep convection to develop. On the large scale, the environment in which wet or dry cold surges form is closely related to the Madden-Julian Oscillation (MJO) phase. Dry and moderate surges occur predominantly in the suppressed phases of the MJO, while wet surges often herald the eastward propagation of the MJO convective envelope. Finally, convectively active phases in the Australian monsoon are more likely following dry cold surges, and are sometimes associated with the MJO.

Plain Language Summary Cold surges are large-scale monsoon weather systems that bring strong north-easterly winds, colder air, and sometimes very heavy rainfall and flooding over the Maritime Continent region between November and March of each year. We investigate the structure and development of dry, moderate, and wet cold surges. The three categories are defined based on rainfall averages over a domain located near the equator. The rainfall, on which the categories are defined, is primarily influenced by the Madden-Julian Oscillation (MJO). The MJO has a major influence on tropical weather on weekly to monthly timescales. Of the three categories, dry surges are characterized by the highest mean sea-level pressure anomalies, and by north-easterly winds that cross the equator into the Southern Hemisphere and then turn to become westerly over Java and northern Australia. The westerly winds are often associated with activity in the Australian summer monsoon. In contrast, wet surges are characterized by low-pressure anomalies over the equator, and weak westerly or easterly winds over southern Java and northern Australia.

1. Introduction

Cold surges are synoptic weather systems that occur over the Maritime Continent during the boreal winter (November–March; NDJFM), and are characterized by the strengthening of prevailing low-level northerly to north-easterly winds, temperature falls of a few degrees over several days, and in some cases, heavy prolonged rainfall and flooding (e.g., Chang et al., 1979, 2004, 2005; Ding, 1994; Fong & Ng, 2012; Johnson & Chang, 2007; S. Y. Lim et al., 2017; MSS, 2022b; Pullen et al., 2015; Ramage, 1971; Tangang et al., 2008; Wu et al., 2007; Xavier et al., 2020). They often produce bursts of convection around the equator, affecting the coastal regions of Southeast Asia such as Vietnam, the Malaysian Peninsula, and Singapore. These regions are located within the western half of the Maritime Continent, which is the largest archipelago on Earth and a region of intense convection (e.g., Argüeso et al., 2020; Neale & Slingo, 2003; Ramage, 1968).

Examples of extreme rainfall from cold surges are documented in Fong and Ng (2012), including one on 9–10 December 1969 where torrential rain fell over the east coast of the Malaysian Peninsula, and a daily rainfall total of 483.1 mm was recorded at Singapore's climate station. During another cold surge on 2 December 1978, a record high daily rainfall total of 512.4 mm was observed, which is about 25% of Singapore's annual average

© 2023. The Authors.

This is an open access article under the terms of the [Creative Commons Attribution License](https://creativecommons.org/licenses/by/4.0/), which permits use, distribution and reproduction in any medium, provided the original work is properly cited.

rainfall (Fong & Ng, 2012). The extreme rainfall from this surge resulted in seven deaths and the evacuation of hundreds due to widespread flooding over the island. More recently, two strong cold surges that affected Singapore and the surrounding region between 1–2 January and 8–13 January 2021 each had peak daily rainfall amounts exceeding 200 mm at Singapore's climate station. These consecutive cold surges were the primary contributors of the second wettest January in 152 years of record (MSS, 2022a).

Cold surges are driven by the strengthening of a large anticyclone over Siberia that dominates the low-level circulation over Asia, often referred to as the “Siberian high” (e.g., Ding, 1994; Fong & Ng, 2012; Lau & Li, 1984; H. Lim & Chang, 1981). Southward intrusions of the Siberian high often result in sudden surges of strong northerly to north-easterly winds that propagate toward China and the South China Sea. As cold and dry winds strengthen with the passage of the surge, the post-surge air crosses higher equatorial sea surface temperatures. Hence, in the post-surge air the evaporation, humidity, and temperature all increase (Chang et al., 1979, 1983). Johnson and Houze (1987) adapted meridional cross sections of temperature and dew point temperature constructed by Warner (1982) to illustrate the gradual transition in the lower troposphere from cold, dry air at 22°N to warm, moist tropical air at 12°N. This transition is associated with large-scale ascent and deep convection that is particularly strong near the Borneo region as a response to strengthening low-level winds, and surface sensible and latent heat fluxes (Chang et al., 1979; Johnson & Zimmerman, 1986; Warner, 1982). In other words, cold and dry surge air that is advected equatorward becomes warm and moist due to surface heat and evaporative fluxes.

Along with strengthening low-level winds, a cyclonic circulation sometimes forms off the northwest coast of Borneo. This circulation is known as the Borneo vortex and is associated with enhanced deep convection (e.g., Chang et al., 1979, 2003, 2005; Johnson & Houze, 1987). H. Lim and Chang (1981) showed that both the north-easterly surge winds and the Borneo vortex are associated with the excitation of Rossby waves as the main response to midlatitude pressure forcing from the Siberian high. Although their study shows that the Borneo vortex can occur even in the absence of topography, other studies have shown that this cyclonic circulation is maintained by the low-level convergence in the region between the north-easterly cold surge winds and the mountainous terrain of Borneo (Chang et al., 2003; Cheang, 1977; Johnson & Houze, 1987; Koseki et al., 2014). According to Koseki et al. (2014), strong cold surges transport high absolute vorticity and water vapor from higher tropical latitudes to the equatorial region, which sustains mesoscale convection and significantly enhances rainfall over the South China Sea.

From November to January, heavy rainfall from cold surges often affects Vietnam, the Malaysian Peninsula, and Singapore (Fong & Ng, 2012; MSS, 2022a). Between February and March, cold surges cross the equator about 75% of the time. The cross-equatorial surge flow is associated with drier conditions over the entire Malaysian Peninsula, eastern Vietnam, and Sumatra, but enhanced rainfall over the Java Sea and northwest of Australia (Xavier et al., 2020). This contrast in cold surge precipitation within the winter monsoon season may be attributed to variations in the Siberian high and Intertropical Convergence Zone (ITCZ). For example, drought conditions over most parts of Indo-China, the Malaysian Peninsula, and Singapore in February 2014 were attributed to a narrower ITCZ that caused convective regions to be restricted to the south of the equator (McBride et al., 2015; Xavier et al., 2020). It is also thought that cross-equatorial surges sometimes trigger the onset of the Australian summer monsoon (e.g., Davidson et al., 1983; Love, 1985; Suppiah & Wu, 1998). Moreover, the relative importance of cross-equatorial surges to bursts in the Australian summer monsoon compared to other influences such as midlatitude fronts and the Madden-Julian Oscillation (MJO; e.g., Berry & Reeder, 2016; Narsey et al., 2017; Narsey et al., 2018) have not yet been investigated.

Yang et al. (2019) is the first study to specifically examine the climatological conditions associated with wet and dry cold surges. They analyzed wet and dry surges over Singapore during NDJFM 1979–1980 to 2017–2018. They found that wet cold surges are characterized by a strengthening of the moisture flux in the South China Sea, positive moisture flux convergence anomalies between 0°N and 10°N two days before surge onset, and that heavy rainfall over Singapore is associated with a cyclonic circulation between Singapore and western Borneo on the day of onset. In contrast, dry surges exhibit negative moisture flux anomalies from 0°N to 15°N and positive anomalies from 0°S to 12°S up to 5 days prior to the surge. Consistent with cross-equatorial surges, these dry surges mostly occur later in the boreal winter season between January and February.

Cold surges lasting six or more days that reach the low latitudes and precipitate over the Maritime Continent region were classified into four types by Abdillah et al. (2021). Of the four surge types, two are relevant to the equatorial Maritime Continent region, namely the “South China Sea type” and “Both type.” The former mostly occurs in the early winter months and is often associated with low-pressure vortices near Borneo leading to heavy

rainfall and flooding over Southeast Asia, whereas the latter is a combination of surges that affect both the South China Sea and the Philippine Sea, and is characterized by the strong southward propagation of both northerly wind and high-pressure anomalies that cross the equator. These surges are also characterized by strong positive precipitation anomalies over the South China Sea, western Maritime Continent, and Java. Additionally, a more recent statistical study by Feng et al. (2022) explored the role of cold surges in triggering the development of El Niño by changing the surface wind over the western equatorial Pacific. Their analysis divided cold surges into the western and eastern types with respect to their pathways in the northwestern Pacific; the western type passes through the South China Sea while the eastern type passes through the Philippine Sea. They find that only the latter could efficiently induce significant surface equatorial westerly anomalies to trigger El Niño.

According to Chang et al. (2005), the MJO modulates the frequency of cold surges and the variability of deep convection. The deep convection is also affected by the interaction amongst the Borneo vortex, cold surges, and the MJO. Chang et al. (2005) find that the presence of cold surges enhances the pattern of increased (decreased) deep convection over the South China Sea when the Borneo vortex is present (absent). Cold surges strengthen the vortex and shift the vortex center from over the South China Sea to the western coast of Borneo. There is strong cyclonic horizontal shear over Borneo associated with enhanced equatorial westerly winds when the convectively active part of the MJO (i.e., phase 3 out of 4 based on Figure 10 of Chang et al., 2005) is centered over the eastern portion of the Maritime Continent. Thus, the MJO may inhibit weak cold surges since its circulation pattern directly opposes the north-easterly cold surge winds. Additionally, the vortex is least likely to be present when the convectively inactive part of the MJO (i.e., phase 1 out of 4 based on Figure 10 of the study) is over the Maritime Continent. Therefore, there are fewer cold surges and vortices during the convectively inactive phases of the MJO.

S. Y. Lim et al. (2017) also studied the effects of cold surges and the MJO on rainfall over Southeast Asia. They found that the active phases of the MJO create a more favorable environment for convection by moistening the atmosphere, which in turn enhances conditional instability. Although less frequent, cold surges during the active phases of the MJO result in higher rainfall and the most extreme rainfall events as reported by S. Y. Lim et al. (2017). Additionally, Xavier et al. (2020) show that cross-equatorial surges in February and March, which are characterized by prolonged periods of strong meridional flow at the equator, tend to reverse the MJO wind fields and hence suppress rainfall in the northern parts of the western Maritime Continent but enhance rainfall over Java. Moreover, the equatorward advection of cold sea-surface temperatures from the midlatitudes by cold surges can also act to suppress convection in the southern parts of the South China Sea.

The local thermodynamics of tropical moist convection can be related to the mid-tropospheric buoyancy in an idealized entraining plume (i.e., the plume buoyancy), which we denote B_L (Ahmed & Neelin, 2018; de Rooy & Siebesma, 2010; Gregory, 2001). Based on this idea, Adames et al. (2021) investigated the relationship between buoyancy and precipitation. They found that over the tropical ocean, precipitation is proportional to the buoyancy of a plume that rises above the deep boundary layer and entrains environmental air through a deep inflow profile as it ascends into the lower-free troposphere. In particular, there is a strong and linear relationship between B_L and precipitation above a threshold value of -0.02 m s^{-2} . In the tropics, this precipitation-buoyancy relationship appears to represent the underlying physical process better than more standard diagnostics such as convective available potential energy (CAPE) and convective inhibition (CIN). Therefore, we use B_L to characterize the environmental thermodynamic conditions for cold surge precipitation, and to determine the differences in B_L in wet and dry surges.

The present paper describes the synoptic structure and development of wet and dry cold surges over the Maritime Continent using observational and reanalysis data sets. Additionally, we analyze the local thermodynamics of the convection associated with cold surges from the perspective of B_L . Section 2 outlines the data and methodologies used. Section 3 investigates the climatologies of the seasonal and diurnal cycles of non-surge days, and dry, moderate, and wet surges. Section 4 contrasts and discusses the synoptic structure of dry, moderate, and wet cold surges using long-term composites. Section 5 analyzes the relationship between the MJO and cold surges, while Section 6 examines the connection between cold surges and the Australian summer monsoon. Conclusions follow in Section 7.

2. Data and Methods

2.1. ERA5 and GPM

Output from the fifth reanalysis of the European Center for Medium-Range Weather Forecasts (ECMWF ERA5; Hersbach et al., 2020) is used to composite long-term observations over a 20-year climatological period from

Table 1
Cold Surge Definition and Criteria Used in This Study

Variable	Condition	Purpose
MSLP	Exceed 1,020 hPa anywhere within 18°N–22°N, 105°E–122°E (brown box in Figure 1)	Ensures that the cold surge winds are forced by the southward extension of the Siberian high rather than local tropical circulations such as typhoons from the Philippine Sea (Ding, 1990; S. Y. Lim et al., 2017; Xavier et al., 2020). In other words, the MSLP condition eliminates surge events that are not related to cold air outbreaks from the Siberian high and removes events with easterly flow from the Philippine Sea
Wind speed at 925 hPa	At least 0.75 standard deviations above the 20-year NDJFM mean when averaged over 5°N–10°N, 107°E–115°E (magenta box in Figure 1)	The wind speed condition is commonly used by operational forecasters to monitor cold surges (S. Y. Lim et al., 2017). The choice of 925 hPa was adapted from Chang et al. (2005)
Wind direction at 925 hPa	Between 337.5° and 90°	Constrains the surge winds from north-north-westerly to easterly

November 2000 to March 2020 (NDJFM 2000–2001 to 2019–2020). The ERA5 data have a horizontal grid spacing of $0.25^\circ \times 0.25^\circ$ and we use 27 vertical levels from 1,000 to 100 hPa. Daily averages of hourly resolution data are computed for the following ERA5 fields: mean sea-level pressure (MSLP), total column water vapor (TCWV), zonal and meridional winds, vertical motion (ω), temperature, and specific humidity. The temperature and specific humidity are also computed at 3-hourly intervals.

We use Global Precipitation Measurement (GPM; Huffman et al., 2019) data to analyze the precipitation over the 20-year period since data are only available from 2000. It has a horizontal grid spacing of $0.1^\circ \times 0.1^\circ$ and the multi-satellite precipitation estimate with gauge calibration field (i.e., “precipitationCal”) is used (Huffman et al., 2019). The data set containing the final estimate of daily accumulated GPM precipitation (i.e., GPM IMERG Final Precipitation L3) is used for the daily mean composites, and 30-min resolution data is used to analyze the diurnal cycle at 3-hourly intervals.

Finally, we use daily data for the MJO index over the entire climatological period, where the real-time multi-variate MJO index (RMM; Wheeler & Hendon, 2004) is used to identify the amplitudes and phases of the MJO.

2.2. Cold Surge Identification

We identify cold surges by applying various criteria from Ding (1990), Chang et al. (2005), and S. Y. Lim et al. (2017), as specified in Table 1.

Based on the ERA5 climatology for NDJFM 2000–2001 to 2019–2020, the horizontal wind speed at 925 hPa must be at least 11.5 m s^{-1} to satisfy the wind speed threshold. The cold surges must also satisfy all three conditions for at least two consecutive days (Ding, 1990). From these conditions on the wind speed and direction, the “South China Sea type” and “Both type” are constrained to be the cold surges from Abdillah et al. (2021). These are also the only surge classifications that affect the Maritime Continent region. In total, the requirement for two consecutive surge days eliminates 40 single-day surges within the 20-year climatological period, leaving a total of 545 cold surge days and 132 surges that are two days or longer.

2.3. Wet Versus Dry Cold Surges

Precipitation quartiles are used to distinguish dry (below the lower quartile—33 surges; 114 days), wet (above the upper quartile—33 surges; 124 days), and moderate (between the quartiles—66 surges; 307 days) cold surges for NDJFM 2000–2001 to 2019–2020. The precipitation thresholds for each category are based on precipitation averages over a domain encompassing Singapore and parts of Malaysia, Sumatra, and Borneo (see the “Precipitation domain,” blue box in Figure 1). The boundary for the lower quartile is approximately 3.5 mm d^{-1} and for the upper quartile it is approximately 17.4 mm d^{-1} . Anomalies for each variable are calculated by subtracting the 31-day centered moving average seasonal cycle climatology. Composites over the 20-year climatology are used to analyze the synoptic-scale structure and development of cold surges, and the environments that characterize the dry, moderate, or wet surges. Lagged composites are computed between day -5 and day $+5$ relative to the surge onset for each cold surge category. Composite maps are plotted within $15^\circ\text{S}–25^\circ\text{N}$, $95^\circ\text{E}–125^\circ\text{E}$ (see the dashed red box in Figure 1) and $5^\circ\text{S}–20^\circ\text{S}$, $95^\circ\text{E}–150^\circ\text{E}$ for the Australian summer monsoon analysis (encompasses the “Australian monsoon domain,” green box in Figure 1).

To assess the statistical significance of each lagged composite, we construct a set of 1,000 composites based on random days. The dates sampled are within ± 7 days from each of the 33 lagged composite days relative to surge onset in the dry and wet categories. Hence, these random composites have the same seasonal distribution as the actual composites. We then assess the statistical significance by determining whether the actual surge composite falls outside of the 5th or 95th percentiles of the mean random composite distribution for each grid point. However, we note that the relevance of significance testing is disputed in atmospheric science and many other disciplines (e.g., Ambaum, 2010; Gill, 1999; Johnson, 1999; Nicholls, 2001), and that any conclusions drawn from such testing must be treated with caution.

2.4. Large-Scale Environment

The relationship between cold surge days in each category and the MJO is also analyzed since the MJO is one of the large-scale organizing structures in the tropical atmosphere. First, the RMM index is used to categorize

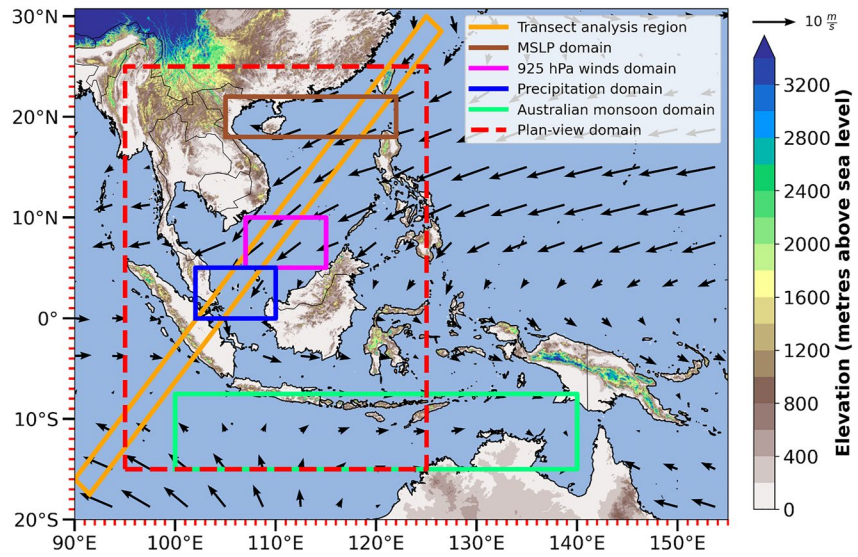


Figure 1. Map of the Maritime Continent region that depicts the transect analysis region (orange box), the cold surge indices domains for mean sea-level pressure (brown box) and horizontal winds at 925 hPa (magenta box), the precipitation domain to contrast wet and dry cold surges (blue box), the composite maps analysis region (dashed red box), and the Australian monsoon domain (green box). Wind vectors at 925 hPa for the NDJFM 2000–2001 to 2019–2020 mean climatology.

days by phase of the MJO. Days with RMM amplitude greater than or equal to 1 are considered to be in one of phases 1–8 as defined by the RMM index, otherwise the days are considered to be non-MJO days. For each surge type, we then calculate the normalized frequency of days in each phase of the MJO. This is defined as the fraction of days within a particular surge category that are in a particular phase of the MJO divided by the fraction of all days in the climatology that are in the same phase of the MJO. For the Maritime Continent, phases 2–3 (phases 5–7) are considered the active (suppressed) phases of the MJO.

2.5. Local Conditions: Plume Buoyancy (B_L)

We also analyze the local thermodynamics of the convection associated with cold surges in each category using B_L . Here we apply the formulation of Adames et al. (2021), in which B_L is defined as:

$$B_L = \frac{g}{\kappa_L} \left(W_B \frac{\theta_{eB} - \theta_{eL}^*}{\theta_{eL}^*} - W_L \frac{\theta_{eL}^* - \theta_{eL}}{\theta_{eL}^*} \right) \quad (1)$$

where

$$\kappa_L = 1 + \frac{L^2 q^*}{c_p R_v T^2}, \quad (2)$$

$$W_B = \frac{\Delta P_B}{\Delta P_L} \ln \left(1 + \frac{\Delta P_L}{\Delta P_B} \right), \quad (3)$$

and

$$W_L = 1 - W_B. \quad (4)$$

In Equation 1, $g = 9.8 \text{ m s}^{-2}$, θ_{eB} and θ_{eL} denote the equivalent potential temperatures within the deep boundary layer (DBL; 1,000 to 850 hPa) and lower free troposphere (LFT; 850 to 600 hPa) respectively, and θ_{eL}^* is the saturation equivalent potential temperature within the LFT. In Equation 2, κ_L is the scaling term, where $L = 2.5 \times 10^6 \text{ J kg}^{-1} \text{ K}^{-1}$ is the latent heat of vaporization, $c_p = 1,004 \text{ J kg}^{-1} \text{ K}^{-1}$ is the specific heat of dry air at constant pressure, $R_v = 461 \text{ J kg}^{-1} \text{ K}^{-1}$ is the gas constant of water vapor, q^* is the saturation specific humidity, and T is the temperature. In Equations 3 and 4, ΔP_B and ΔP_L denote the pressure thickness of the DBL and LFT (150 and 250 hPa) respectively.

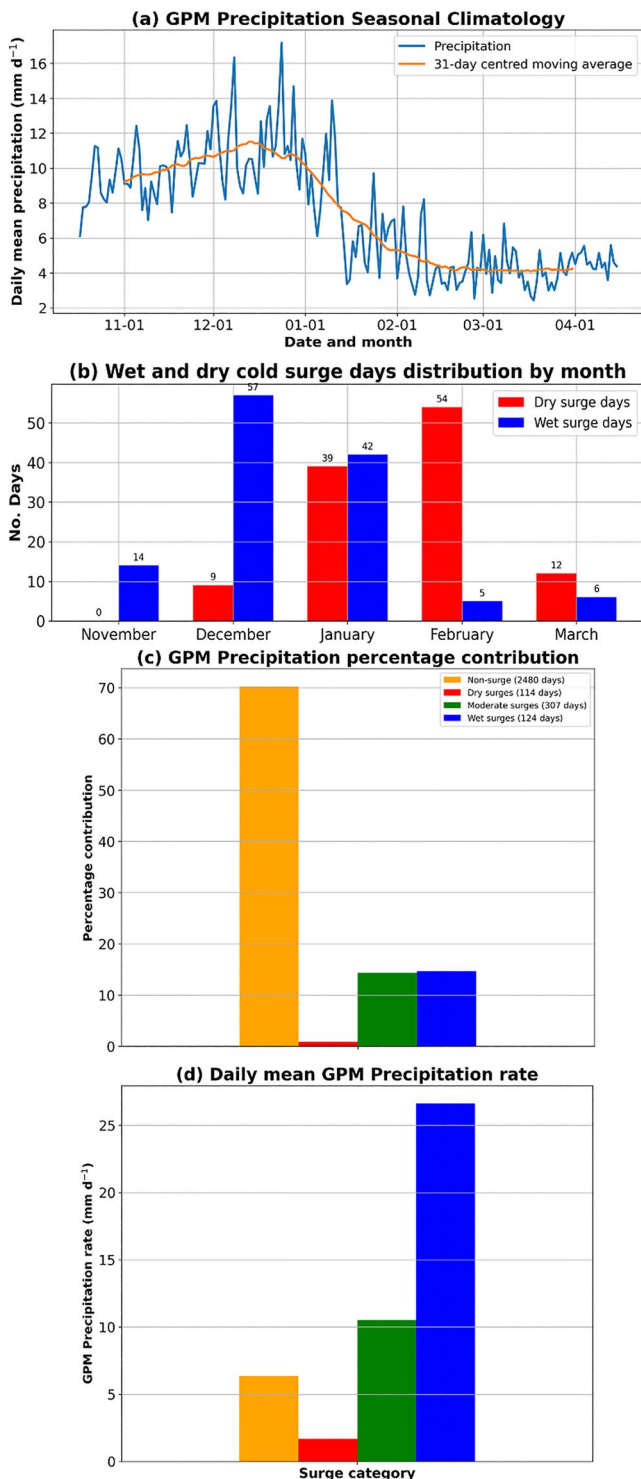


Figure 2. (a) Seasonal cycle of daily mean Global Precipitation Measurement (GPM) precipitation from 1 November to 31 March (blue lines) with 31-day centered moving average curves (orange lines) averaged over 2000–2001 to 2019–2020. (b) Distribution of dry (red bars) and wet (blue bars) cold surge days by month over the NDJFM season. (c) GPM precipitation percentage contribution and (d) daily mean GPM precipitation rates. Non-surge days (orange), and dry (red), moderate (green), and wet (blue) cold surge days.

B_L is defined in terms of equivalent potential temperature (θ_e), which is approximately conserved during moist adiabatic processes. Adames et al. (2021) interpret B_L as a measure of the buoyancy of an air parcel as it rises to the top of the LFT layer, mixing with its environment. Therefore, B_L is a measure of convective instability of the lower troposphere that accounts for the effects of mixing. There are two terms in Equation 1, each given a weighting W_B or W_L . The first term is the “undilute B_L ”, which is a traditional measure of the convective instability of the lower troposphere (Adames et al., 2021; Raymond et al., 2015). For this measure of convective instability, the parcel is assumed not to mix as it passes through the LFT. Positive values of undilute B_L indicate unstable profiles with a high potential for convection, provided air is lifted from the boundary layer (i.e., the DBL at 850 hPa) without mixing with its environment. The second term is a function of the saturation deficit of the LFT, and represents the reduction in buoyancy in a rising plume as it entrains and is diluted by free-tropospheric air. The importance of the second term is set by the weights W_B and W_L , which describe the relative mass inflow to the plume from the DBL and LFT. For the parameters used here (taken from Adames et al., 2021), $W_B = 0.59$ and $W_L = 0.41$.

As B_L increases from negative values toward zero, the precipitation increases exponentially (see Figure 3 of Adames et al. (2021)). A critical value of -0.02 m s^{-2} marks the beginning of a regime wherein the precipitation increases linearly and rapidly with increasing values of B_L . Although B_L is averaged between 15°N and 15°S in the Adames et al. (2021) study, here we compute B_L over the precipitation domain.

3. Climatologies of the Seasonal and Diurnal Cycles

3.1. Seasonal Cycle of Wet and Dry Cold Surges

There is a clear seasonal cycle in GPM precipitation, which is averaged over the precipitation domain and during NDJFM. The 31-day centered moving average precipitation peaks at approximately 11.5 mm d^{-1} in the middle of December, and is lowest at approximately 4.1 mm d^{-1} in early March (Figure 2a). Most wet surge days are also found in December and January (57 and 42 days respectively) while most dry surge days are found in January and February (39 and 54 days respectively; Figure 2b).

In the 20-year period of the analysis, there are cold surges on approximately 18% of days (545 surge days out of 3,025 days), yet cold surges contribute to approximately 30% of total rainfall. The wet and moderate surges account for approximately 14.7% and 14.3% of the total rainfall contribution respectively, with less than 1% from the dry surge days (Figure 2c). The higher contribution of rainfall from cold surges relative to the fraction of cold surge days within the 20-year period is consistent with the overall higher daily mean rainfall rate during cold surge days (approximately 12.3 mm d^{-1} for all surge days and 10.5 mm d^{-1} for moderate surges) than non-surge days (approximately 6.4 mm d^{-1} ; Figure 2d). Thus, cold surges are associated with higher precipitation on average over the precipitation domain, which is consistent with the cold surge air becoming warmer and moister from surface heat and evaporative fluxes as it is advected equatorward. Dry and wet surges also have a daily mean rainfall rate of approximately 1.7 and 26.6 mm d^{-1} respectively. When the seasonal cycle is removed, there are individual days within the wet surge category that fall below the climatological mean (20 out of 124 days) and vice versa for dry surges (7 out of 114 days). This is expected since the precipitation quartiles for each surge category are based on the mean precipitation of entire cold surges rather than individual cold surge days.

3.2. Diurnal Cycle of Plume Buoyancy and GPM Precipitation

There is an approximately exponential relationship between daily mean values of B_L and GPM precipitation averaged over the precipitation domain on individual days for non-surge days and each of the three surge categories (Figure 3a). Most wet surge days (119 out of 124 days) exceed the -0.02 m s^{-2} threshold for B_L while most dry surge days (94 out of 114 days) fall below the threshold. Overall, the cold surge days are closer to the threshold, but this may be partly due to the smaller sample size (545 days) compared to non-surge days (2,480 days).

In terms of the diurnal cycle, both the hourly precipitation rate (Figure 3b) and B_L (Figure 3c) over the precipitation domain are highest in the wet surge composites, followed by the moderate, non-surge, and dry composites. In the wet and moderate surge composites, GPM precipitation peaks at 1400 LST (approximately 1.31 and 0.509 mm hr^{-1} respectively) and the diurnal contrasts are more pronounced. The precipitation rates at 0500 LST for the wet and moderate composites (approximately 1.17 and 0.505 mm hr^{-1} respectively) are also well above the daily mean values (approximately 1.11 and 0.44 mm hr^{-1} respectively), unlike the non-surge and dry surge composites, which is most likely because of offshore precipitation during the nocturnal hours. The precipitation rate peaks between 1400 LST and 1700 LST in the non-surge composites (approximately 0.33 mm hr^{-1}), and at 1700 LST in the dry surge composites (approximately 0.09 mm hr^{-1}). On the other hand, minima in the diurnal cycle occur at 2300 LST for both the wet surge and non-surge composites (approximately 0.91 and 0.20 mm hr^{-1} respectively), between 2000 LST and 2300 LST in the dry surge composites (approximately 0.05 mm hr^{-1}), and 2000 LST in the moderate surge composites (approximately 0.31 mm hr^{-1}). In contrast, there is a daytime peak of B_L at 1400 LST in all cases, and a greater peak at 0500 LST in the wet and moderate surge composites (approximately -0.022 and -0.038 m s^{-2} respectively) since nocturnal convection occurs over the ocean in these cases. There are nocturnal minima at 2000 LST for all categories but 2300 LST in the dry surge composites, and lower minima at 0800 LST for the dry and moderate surge composites (approximately -0.074 and -0.044 m s^{-2} respectively).

These results show that the diurnal cycle of B_L , which is based on ERA5, is consistent with that of the GPM precipitation anomalies. They suggest that the convective onset, and hence the diurnal precipitation patterns, are controlled by B_L . Moreover, most cold surges, particularly wet surges, are characterized by a moister free troposphere than non-surge days over the precipitation domain, which reduces the effect of entrainment and allows convection to penetrate through the lower troposphere. This implication will be further investigated in the lagged composite analyses of the cold surge synoptic structure in the next section.

4. Synoptic Structure and Development of Cold Surges

4.1. The Development of Cold Surges Over the Maritime Continent

In this section, we investigate the synoptic environments of each cold surge category using lagged composite anomalies of TCWV (Figure 4), and ω at 700 hPa (Figure 5). The horizontal wind anomaly vectors at 925 hPa are also shown on each map to mark the development of the low-level surge winds, and ω is plotted at 700 hPa which is above the topography in the region. In Figure 4, contours of TCWV are drawn at 46, 48, and 50 mm. According to Mapes et al. (2018), the 48 mm TCWV contour encloses the region over the tropical ocean in which convection is found.

In all three surge categories, the north-easterly wind anomalies are consistently strongest on day +1. The dry surge composites are characterized by cross-equatorial flow that reaches equatorward to Java, with westerly anomalies around Java. The wet surge composites feature a cyclonic circulation anomaly between Borneo and the Malaysian Peninsula, which is the Borneo Vortex. The moderate surge composites (not shown) depict weaker cross-equatorial flow and westerly anomalies over Java compared to the dry surge composites. Overall, the horizontal wind patterns are consistent with the Yang et al. (2019) study (see their Figures 4 and 5).

Negative TCWV anomalies from the cold surge extend to the equator in the dry surge composites (-1 to -5 mm), transitioning to positive anomalies around Java ($+1$ to $+2$ mm; Figures 4a and 4b). These negative anomalies cover almost the entire precipitation domain and most of the South China Sea by day -1 and are statistically significant over most of the region. The dry anomalies strengthen and peak under -7 mm to the northeast of Taiwan on day +1 as the cold surge reaches its peak, while the strengthening cross-equatorial flow coincides with the positive anomalies over Java. Areas of statistical significance cover the entire South China Sea and most of the precipitation domain. Moreover, in close to half the precipitation domain the TCWV falls below the 48 mm threshold, which is consistent with the lack of precipitation in this region. In the wet surge composites

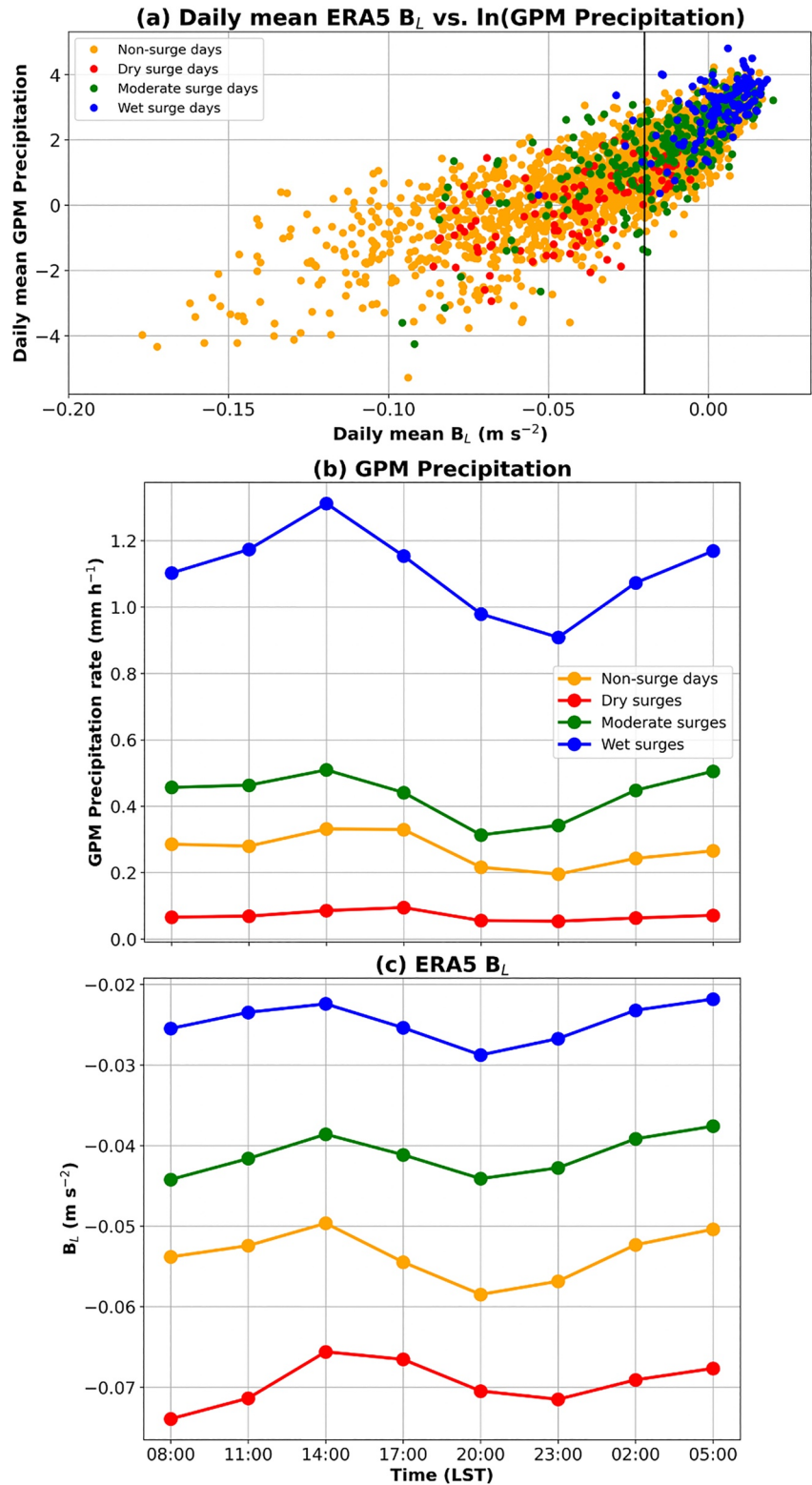


Figure 3. (a) Daily mean B_L versus the natural log of daily mean Global Precipitation Measurement (GPM) precipitation (where the precipitation is exponential in mm d^{-1}) over the precipitation domain in NDJFM 2000–2001 to 2019–2020. The vertical black line is drawn at the -0.02 m s^{-2} boundary for B_L . Diurnal cycle of mean (b) GPM precipitation rate and (c) B_L . Non-surge days (orange), and dry (red), moderate (green), and wet (blue) cold surges.

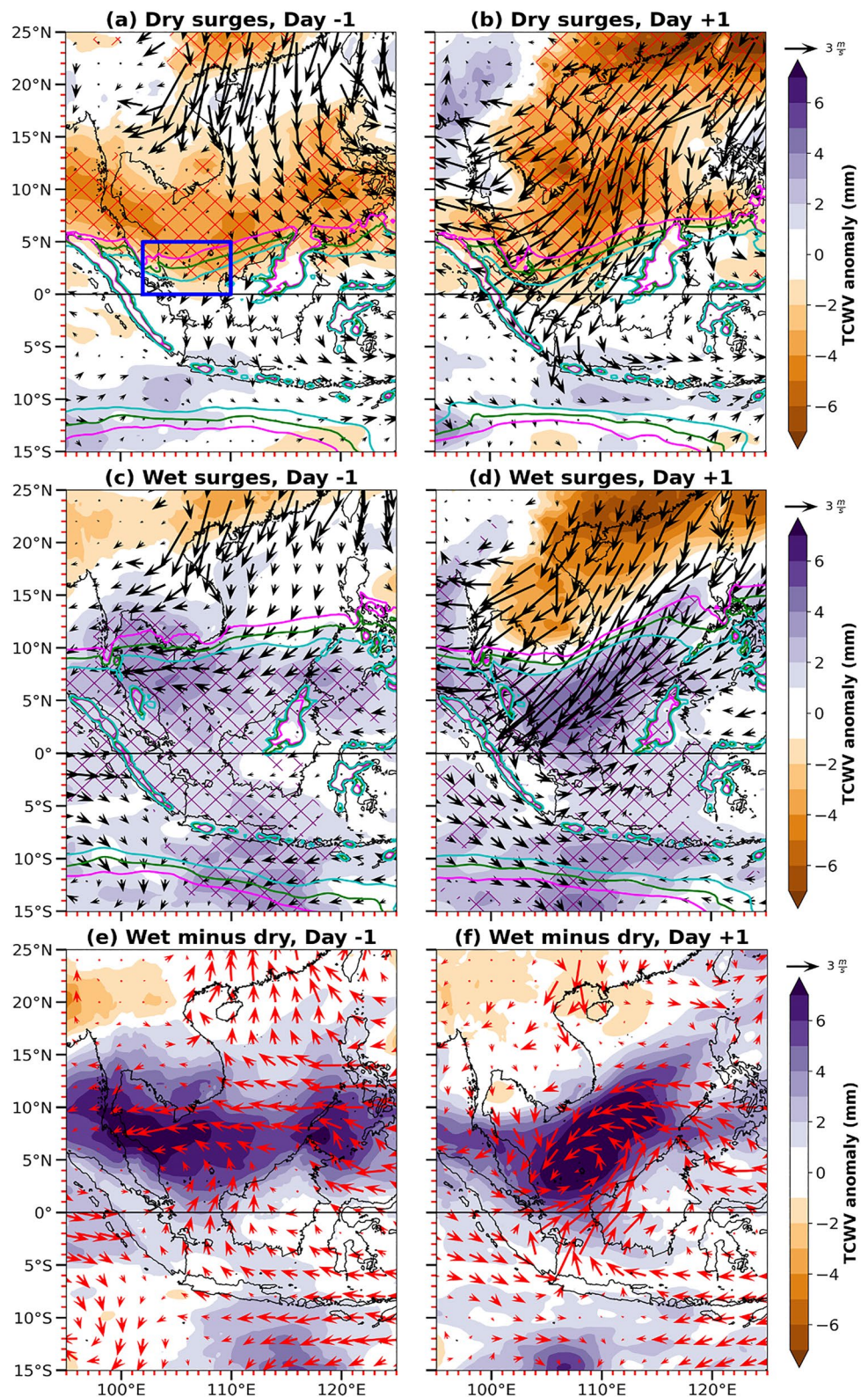


Figure 4. Lagged composite maps of daily mean total column water vapor (TCWV) anomalies with the seasonal cycle removed. Daily mean 925 hPa horizontal wind anomaly vectors. (a, b) Dry and (c, d) wet surges. The red (purple) hatching depicts areas where TCWV anomalies are under (above) the 5th (95th) percentile in the dry (wet) surges. Magenta, green, and cyan contours of TCWV are drawn at 46, 48, and 50 mm respectively. (e, f) Wet minus dry cold surges. Day -1 (left column) and day $+1$ (right column) relative to surge onset. The precipitation domain is depicted by the blue box.

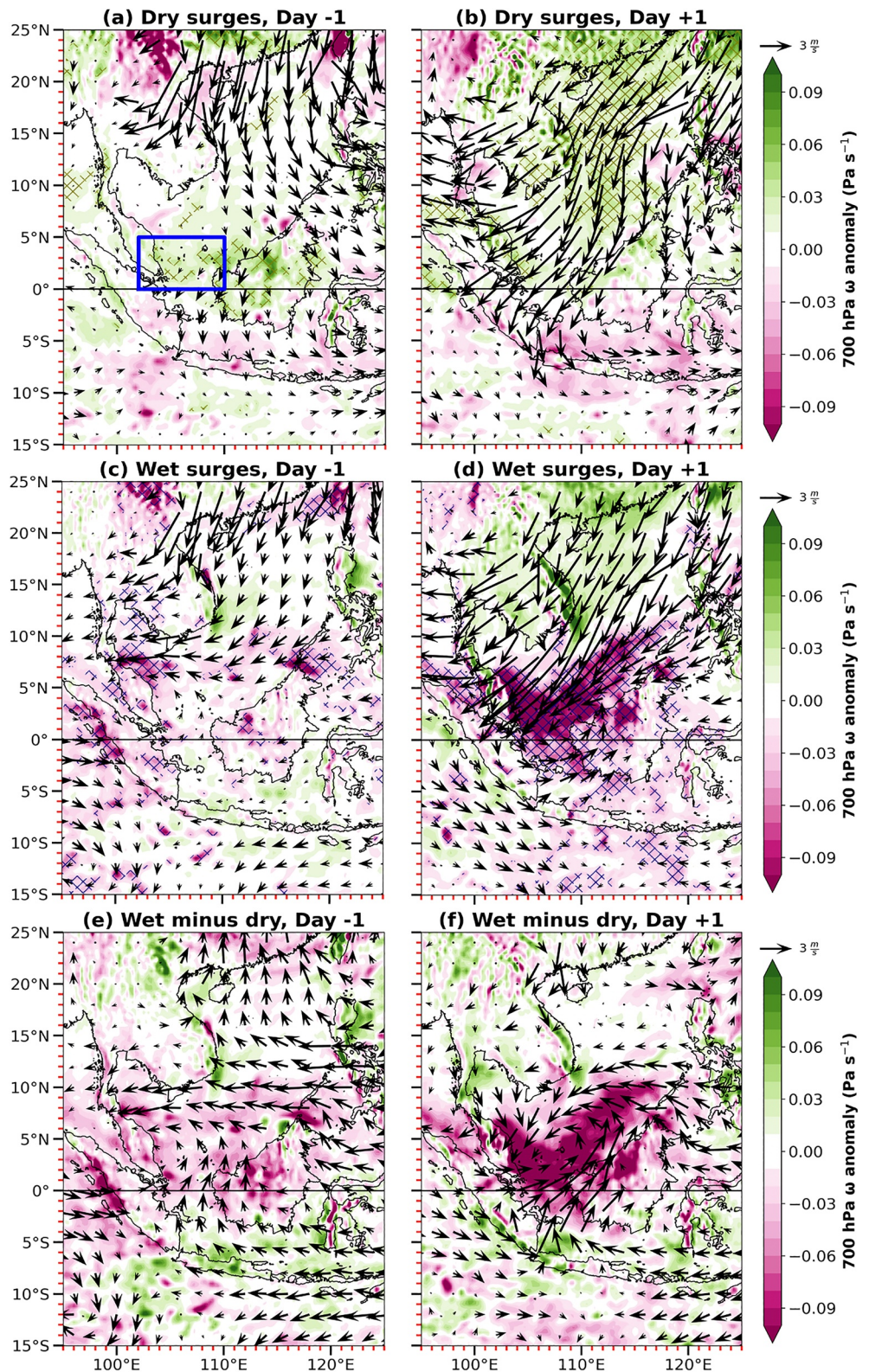


Figure 5. Lagged composite maps of daily mean 700 hPa ω anomalies with the seasonal cycle removed. Daily mean 925 hPa horizontal wind anomaly vectors. (a, b) Dry and (c, d) wet surges. The navy (green) hatching depicts areas where ω anomalies are under (above) the 5th (95th) percentile in the wet (dry) surges. (e, f) Wet minus dry cold surges. Day -1 (left column) and day +1 (right column) relative to surge onset. The precipitation domain is depicted by the blue box.

(Figures 4c and 4d), widespread positive TCWV anomalies are already evident prior to surge onset (+2 to +4 mm) and absolute TCWV values are well above 48 mm over the entire precipitation domain. A meridional TCWV anomaly gradient is found on day +1, ranging from close to +5 mm over the equator to -7 mm over the northern South China Sea. This sharp gradient is consistent with the convection near the equator in contrast to drier surge air over the northern South China Sea. The moist anomalies are also statistically significant on both day -1 and day +1 over the entire precipitation domain and its surroundings. Weaker TCWV anomalies are found in the moderate surge composites (not shown) on day -1 over the precipitation domain and much of the South China Sea (-3 to +1 mm). The TCWV still exceeds 48 mm over the precipitation domain although the threshold to the north of the domain is located closer to the equator (around 6°N to 8°N) compared to the wet cases (around 8°N to 10°N). On day +1, the anomalies follow a similar pattern to that of the wet surge composites, although the meridional moisture gradient is weaker, ranging from approximately +3 mm at the equator to -5 mm over the northern South China Sea. The largest positive TCWV anomaly differences between the wet and dry composites on day -1 (peaking over 7 mm; Figure 4e) generally cover the statistically significant regions in both the dry and wet surges. Areas with the largest differences on day +1 (Figure 4f) are associated with the Borneo Vortex between the Malaysian Peninsula and Borneo.

In each cold surge category, dry air from the surge is accompanied by positive ω anomalies at 700 hPa (i.e., stronger descent or weaker ascent relative to climatology), particularly on day +1. Positive anomalies associated with the surge over Southern China are most widespread in the dry surge composites (peaking close to +0.10 Pa s⁻¹), and weaker anomalies are observed over most of the South China Sea (+0.00 to +0.03 Pa s⁻¹). These positive anomalies strengthen between day -1 (Figure 5a) and day +1 (Figure 5b), and negative anomalies strengthen over Java (-0.01 to -0.06 Pa s⁻¹ over most parts). The positive anomalies on day +1 are statistically significant over most of the South China Sea and parts of the Malaysian Peninsula, and are largely consistent with the negative TCWV anomalies in Figure 4b. From day -1, areas of enhanced ascent are already evident over much of the equatorial South China Sea in the wet surge composites (peaking under -0.10 Pa s⁻¹; Figure 5c). Large areas of strongly enhanced ascent that are statistically significant develop and strengthen by day +1 (under -0.10 Pa s⁻¹ over most of the precipitation domain; Figure 5d). In the moderate surge composites (not shown), the 700 hPa ω anomalies are relatively weak over the precipitation domain on day -1 (-0.04 to +0.04 Pa s⁻¹). The anomaly patterns also follow a similar structure to the wet surge composites on day +1, with enhanced ascent over the precipitation domain (peaking close to -0.10 Pa s⁻¹). The largest differences between the wet and dry composites (Figures 5e and 5f) are evident on day +1 (peaking well under -0.10 Pa s⁻¹), which is also associated with the Borneo Vortex.

Cold surges over the northern South China Sea are characterized by below average moisture, and enhanced descent. Dry surges are generally characterized by cross-equatorial flow, stronger descent or weaker ascent, and negative TCWV anomalies that reach the precipitation domain as consistent with lower values of B_L (see Figure 3c). Relatively moist air and enhanced ascent are also found over Java. On the other hand, the cyclonic circulation anomaly, enhanced ascent over the precipitation domain, and the moist anomalies associated with a strong meridional TCWV anomaly gradient are consistent with higher values of B_L in the wet surges. The cyclonic circulation anomaly in Figures 4f and 5f imply a strengthening of surge winds over the Malaysian Peninsula and a weakening over Borneo. This vortex coincides with upward motion and is presumably associated with the stretching of absolute vorticity. The anomalies on the south-eastern flank over Borneo oppose the north-easterly surge flow and prevents cross-equatorial flow, which is a key difference between the wet and dry surge composites. These results are also consistent with the studies which concluded that the vortex is maintained by low-level convergence associated with the convection (Chang et al., 2003; Cheang, 1977; Johnson & Houze, 1987; Koseki et al., 2014). In the days prior to the onset of wet surges, moist anomalies are already present over most parts of the South China Sea (Figures 4c and 4e; days before day -1 not shown). In contrast, dry anomalies spread from the Philippines and its surroundings and strengthen over the South China Sea in the days prior to the dry surge onset (Figure 4a; days before day -1 not shown), merging with the stronger dry anomalies from the surge by the onset.

4.2. Transect Analysis of Cold Surges

ERA5 data are also averaged over 7 transects that are spaced at 0.25° along the South China Sea (see the “Transect analysis region”, orange box in Figure 1). Nearest-neighbor interpolation is performed for each variable along each transect at the same horizontal resolution. The north-easterly component of the along-transect wind anomalies at 925 hPa depict a rapid acceleration of negative anomalies toward the equator in cold surges from about day -2 (Figure 6a). Wind anomalies peak under -5 m s⁻¹ on day +1 when the surge is strongest. Statistically

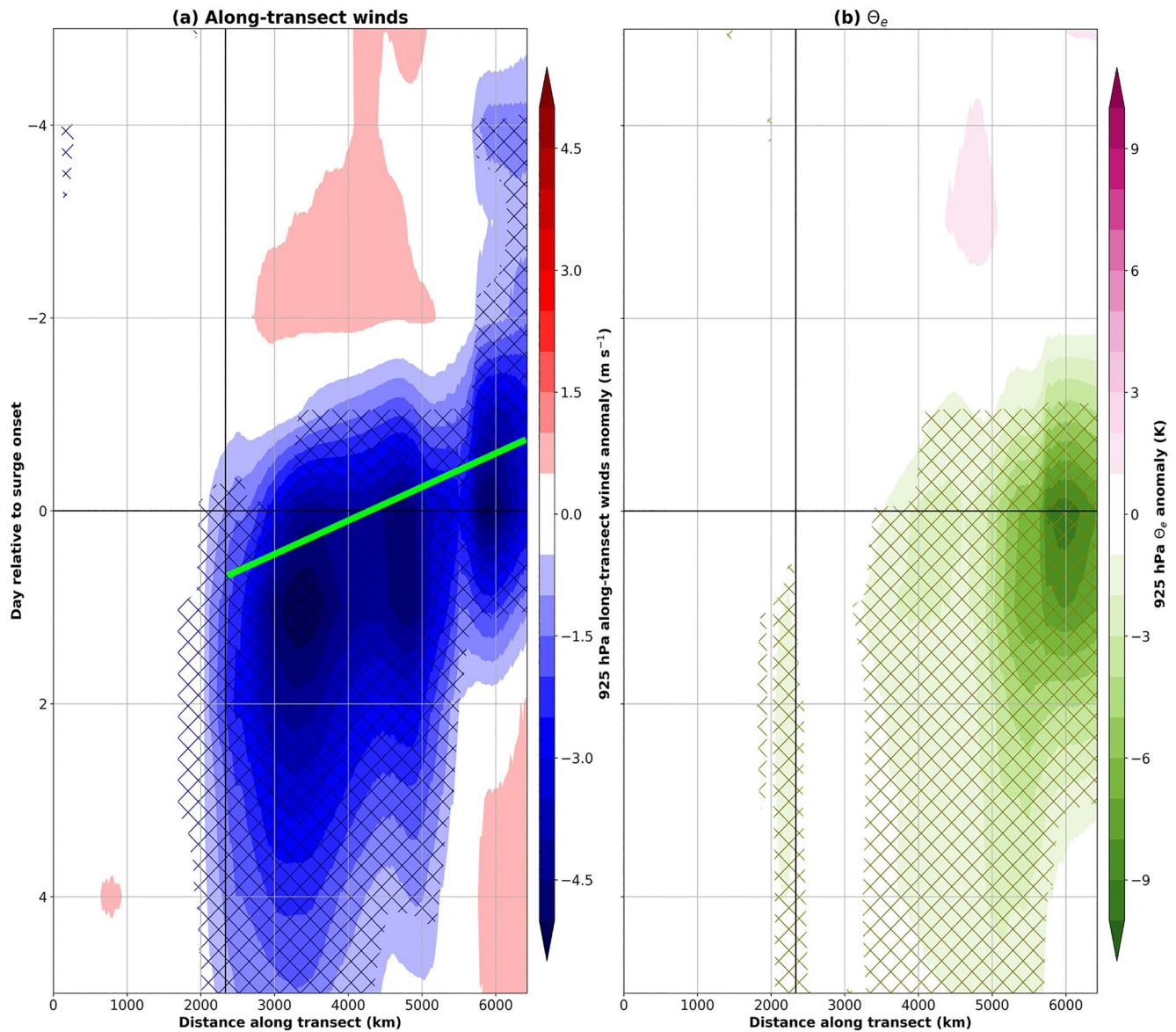


Figure 6. Lagged composite plots of transect-averaged daily mean anomalies of 925 hPa (a) along-transect winds and (b) θ_e from day -5 to day $+5$ relative to surge onset with the seasonal cycle removed. The mean of all 132 cold surges is taken. The transects are averaged over the orange box in Figure 1. The hatching depicts areas where the data is below the 5th percentile. The approximate location of the equator is marked by the vertical black line, and the transects are constructed from south-west to north-east moving left to right. Along-transect winds are negative moving north-east to south-west. The green line indicates the approximate speed of the north-easterly surge wind propagation.

significant regions (above the 95th percentile since the colourbar is flipped) are confined to the north of the transect between day -4 and day -2 , spread equatorward by day -1 , and cross the equator from day 0 onwards. The θ_e anomalies at 925 hPa reflect both the temperature and moisture anomalies (Figure 6b). Overall, negative anomalies of θ_e at 925 hPa (i.e., cold and dry anomalies; peaking close to -10 K), associated with the Siberian high outflow, are spread more slowly toward the equator (approximately 5 m s^{-1}) compared to the propagation of north-easterly winds (approximately 30 m s^{-1}). The negative anomalies are statistically significant (under the 5th percentile) from day -1 . As the composite transect for each of the individual dry, moderate, and wet composites are very similar, only a single composite of all 132 cold surges is shown here.

These results are consistent with the theoretical framework of H. Lim and Chang (1981), who described the development of the surge as the leading edge of a wave packet; in the reanalysis the wind field adjusts quickly and is consistent with the propagation of a wave whereas the air mass spreads more slowly through advection. The

reanalysis is also qualitatively consistent with the Rossby adjustment problem on the beta plane investigated by H. Lim and Chang (1981), where the establishment of the Rossby wave group from the Siberian high explains the development of the north-easterly wind flow. Chang et al. (1983) take the theoretical framework of H. Lim and Chang (1981) and show that cold surges develop in two distinct stages. The first stage is characterized by a significant rise in surface pressure at the cold surge edge and gravity-wave type motions associated with equatorial propagation at about 40 m s^{-1} . The second stage features a sharp decrease in surface dew point temperature accompanied by a decrease in surface temperature that are associated with the passage of a cold front. Following the two stages, the surface wind strengthens, often with a northerly acceleration (Chang et al., 1979, 1983). Therefore, the equatorward propagation of the surge may be viewed as part of the transient motion of the pressure-wind imbalance, resulting in the faster propagation speed of north-easterly winds relative to the slower advection velocity of negative 925 hPa θ_e anomalies in our cold surge composites.

The vertical structure of the θ_e anomalies are compared for each cold surge category (Figure 7). The component of wind along the transect and ω are also plotted. ω is exaggerated by a factor of 50. In all cases, descent and negative θ_e anomalies deepen up to approximately 350 hPa, and strengthen between day -1 and day $+1$ (particularly within the lower troposphere). The cold and dry anomalies are largest in the dry surge composites (peaking under -7 K ; Figures 7a and 7b) and are statistically significant over large areas. Toward the north-eastern end of the transect, north-easterly winds extend from the surface to approximately 800 to 750 hPa before shifting to south-westerly aloft.

Areas of convergence and ascent at the lower levels (with divergence toward the upper troposphere) correspond to positive low-level θ_e anomalies and enhanced precipitation anomalies. Descent and negative θ_e anomalies are associated with negative precipitation anomalies. Two regions of cold and dry anomalies are observed on day -1 over most of the South China Sea in the dry surge composites (-1 to -6 K), which are consistent with the TCWV anomalies in Figure 4a. Warm and moist anomalies are observed in the wet surge composites up to approximately 12°N ($+1$ to $+2 \text{ K}$; Figure 7c). In both the dry and wet categories, the anomalies that are close to the equator extend up to approximately 300 and 250 hPa, respectively. On day $+1$ of the wet composites, positive θ_e anomalies become more widespread along the South China Sea and deepen, reaching close to 200 hPa ($+1$ to $+3 \text{ K}$; Figure 7d). The anomalies near the equator are statistically significant on both day -1 and day $+1$. The precipitation anomalies are highest (peaking close to $+50 \text{ mm d}^{-1}$) just to the north of the equator where positive θ_e anomalies and ascent are strongest. In the moderate surge composites (not shown), both the cold and dry anomalies from the surge (up to -7 K at the northeastern end of the transect), and warm and moist anomalies ($+1$ to $+2 \text{ K}$) near the equator follow a similar pattern to that of the wet surge composites. From the difference between the wet and dry composites (Figures 7e and 7f), positive differences in θ_e anomalies (peaking close to $+7 \text{ K}$ on day $+1$) are associated with stronger north-easterly winds and ascent particularly between 3,000 and 4,000 km along the transect (approximately 5°N and 12°N respectively) when compared to the dry surges. There are weaker north-easterly winds just to the north of the equator, which is consistent with limited cross-equatorial flow in the wet surges. Consistent with the TCWV anomalies in Figures 4c and 4e, much of the South China Sea is characterized by a relatively warm and moist environment prior to the onset of the wet surges.

5. Cold Surges and the MJO

Having examined the local initiation of convection and development of rain through the lens of plume buoyancy, and the synoptic-scale structure and development of the surges, we turn our attention now to the regional scale. We begin with the normalized frequency of cold surge days in each phase of the MJO (including non-MJO days where $\text{RMM} < 1$) relative to climatology for the three surge categories (Figures 8a–8c). There is a clear connection between the phase of the MJO and the number of dry or wet surge days, although surges in each category are found in all phases of the MJO. Dry surge days have normalized frequencies that peak at approximately 2.4 and 2.2 in phases 6 and 7 respectively (Figure 8a), whereas wet surge days have peaks at approximately 2.7 and 2.6 in phases 2 and 3 respectively (Figure 8b). For moderate surge days (Figure 8c), the normalized frequency is lowest in phase 3 (approximately 0.3) and highest in phase 8 (approximately 1.6). In this category, the frequencies of the active phases are relatively low whereas those of the suppressed phases are relatively high. In phases 5–8, the normalized frequencies are all greater than 1. These findings agree with the studies by Chang et al. (2005) and S. Y. Lim et al. (2017) who reported southwesterly anomalies over a large area of East Asia and the western Pacific during phases 2 and 3. According to S. Y. Lim et al. (2017), these anomalies are consistent with the Rossby wave response to the MJO convection pattern, which partially oppose the north-easterly cold surge winds. There are relatively few non-MJO days in both the dry and wet surges, the normalized frequencies being approximately 0.6 and 0.5 respectively.

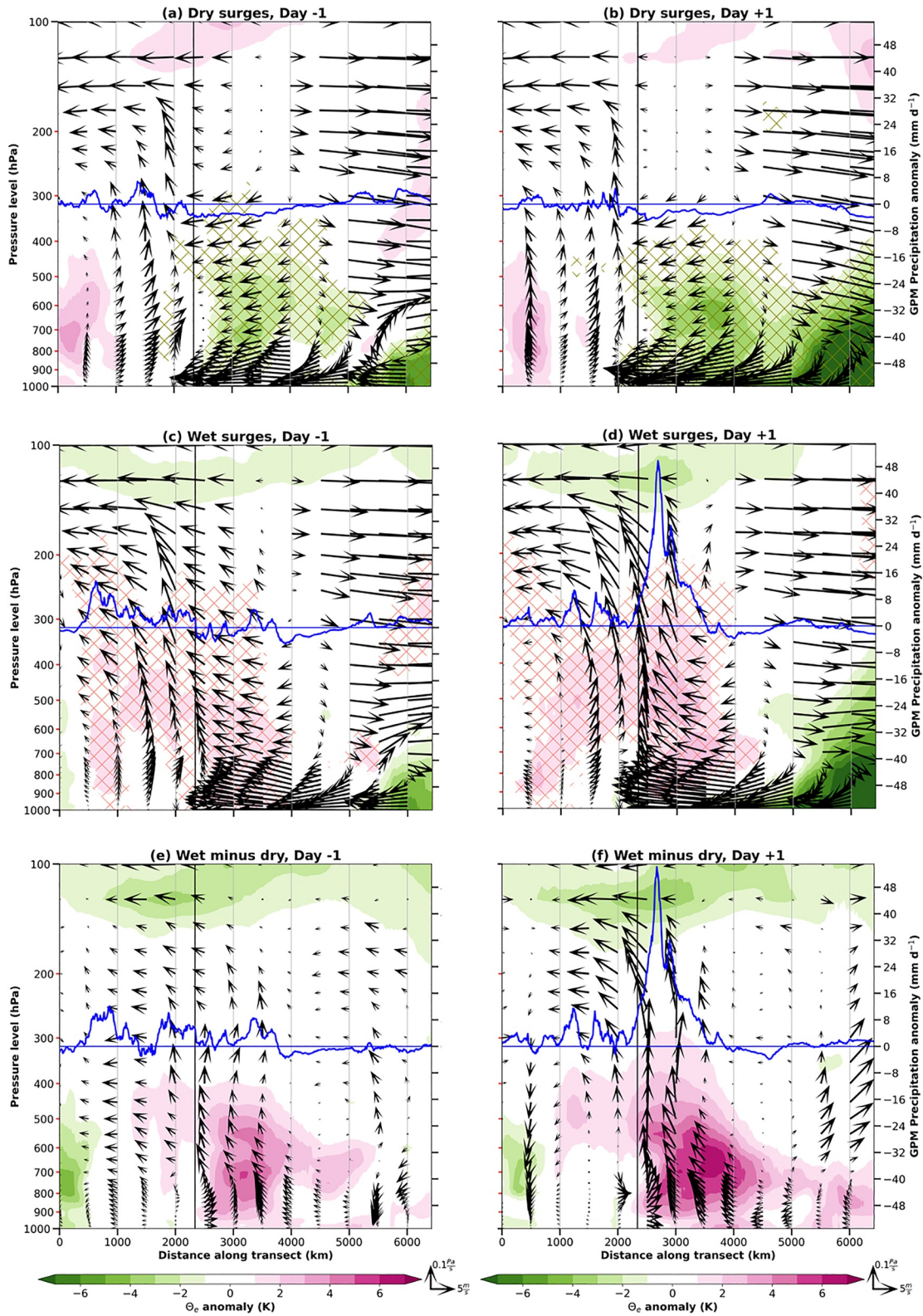


Figure 7.

Lagged composites of the percentage frequency of MJO occurrence in a given phase are shown from day -30 to day $+30$ for each category to illustrate the relationship between cold surges and the MJO (Figures 8d–8f). We only plot the high-amplitude phases of the MJO (where $RMM \geq 1$) since the results change little when the low-amplitude phases are included, and the MJO signal is a little clearer when the low-amplitude phases are excluded. Close to 25% of dry surge onsets are in phase 6 (Figure 8d), and by day $+3$, the peak frequency, which is over 30%, is in phase 7. There is also a tendency for the moderate surges to begin in the suppressed phases, with the peak in phase 5; they account for approximately 15% (Figure 8f). There is a later peak in phase 7, about 15–16 days after the onset, with close to 25% of days. For the wet surge composites, there is a peak of close to 30% in phase 3 of the MJO, 1 day after surge onset, with subsequent peaks in phase 4 on day $+7$, phase 5 on days $+13$ to $+14$, phase 6 on day $+18$, and phase 7 on day $+24$ (Figure 8e). In all cases, the MJO phase in which the peak frequency occurs progresses uniformly from west to east. These results show that the dry and moderate surges occur predominantly in the suppressed phases as part of the eastward propagation of the MJO convective envelope. On the other hand, the MJO in phases 2–3 already exists up to 12 days before the onset of wet surges between 9% and 18% of the time, and the frequency increases by close to a factor of 2 after the onset. In other words, between 18% and 30% of the time, the wet surges appear to trigger the MJO, and to signal the start of the eastward propagation of the MJO convective envelope.

To better understand the relationship between the MJO and the category of cold surge, composites of daily mean MSLP anomalies are made (Figure 9). We compare composites of the active (suppressed) phases of the MJO (phases 2–3 and 5–7 respectively) for all surges to those for the wet (dry) surges. Another set of composites are made for all other phases of the MJO (including non-MJO days) in both surge categories to expose the effect of removing the dominant MJO signal. The magnitude of the horizontal gradient of the MSLP is also computed to check if the synoptic-scale winds are in geostrophic equilibrium.

In all cases, the north-easterly wind anomalies defining the cold surge are consistently associated with positive MSLP anomalies, which are strongest at the northernmost part of the region over inland Southern China (peaking over $+5.0$ hPa in the dry surge composites). The spatial pattern of MSLP and 925 hPa horizontal wind anomalies are almost identical in the dominant MJO phases when comparing the composites for all surge days to those for the dry and wet surges (Figures 9a, 9b, 9d, and 9e), although the contrast between the suppressed and active phases are slightly stronger when specifically comparing the dry and wet surges. Moreover, the surge winds are almost perpendicular to the isobars and in the direction of the MSLP horizontal gradient, and are therefore almost entirely ageostrophic. The gradient magnitude also decreases when moving equatorward along the South China Sea, which is associated with the propagating surge winds. The $+1.0$ hPa MSLP anomaly contour further north (see Figures 9d–9f) shows that the winds are closer to geostrophic equilibrium toward the northern South China Sea.

In the dry surge composites (Figures 9b and 9c), the $+1.0$ hPa MSLP anomalies cross the equator and extend to Java (as with the cross-equatorial wind flow), and approximately mark the leading edge of the surge. These circulation patterns are characteristic of the “Both type” surges in Abdillah et al. (2021). There are widespread westerly anomalies over Java in phases 5–7 of the MJO and weak low-pressure anomalies (approximately -0.5 hPa) to the south-east of the domain (Figure 9b). In these suppressed phases of the MJO (Figures 9a and 9b), the 0.15 hPa deg^{-1} horizontal gradient contour coincides with the approximate location of the turning of the surge winds that cross the equator. Widespread high-pressure anomalies are found outside the suppressed phases, with no westerly anomalies over Java (Figure 9c).

On the other hand, the $+1.0$ hPa contour in the wet surge composites (Figures 9e and 9f) is confined to north of 10°N , which is characteristic of the “South China Sea type” surge in Abdillah et al. (2021). Positive MSLP anomalies extend further equatorward outside the active phases of the MJO and there are weak westerly anomalies over Java (Figure 9f). During the active phases of the MJO, there are weak low-pressure anomalies (-0.5 to -1.0 hPa) over most of the precipitation domain, Java, and the Indian Ocean, and there are easterly anomalies over Java (Figure 9e). There is also a cyclonic circulation anomaly between the Malaysian Peninsula and Borneo

Figure 7. Lagged composite plots of transect-averaged daily mean ERA5 θ_e anomalies from 1,000 to 100 hPa (shading) and daily mean Global Precipitation Measurement precipitation anomalies (blue lines) with the seasonal cycle removed. (a, b) Dry and (c, d) wet surges. The green (orange) hatching depicts areas where θ_e anomalies are under (above) the 5th (95th) percentile in the dry (wet) surges. (e, f) Wet minus dry cold surges. Day -1 (left column) and day $+1$ (right column) relative to surge onset. Vectors depict the magnitudes of daily mean along-transect winds and ω . ω is exaggerated by a factor of 50. The transects are averaged over the orange box in Figure 1. The approximate location of the equator is marked by the vertical black line, and the transects are constructed from south-west to north-east moving left to right.

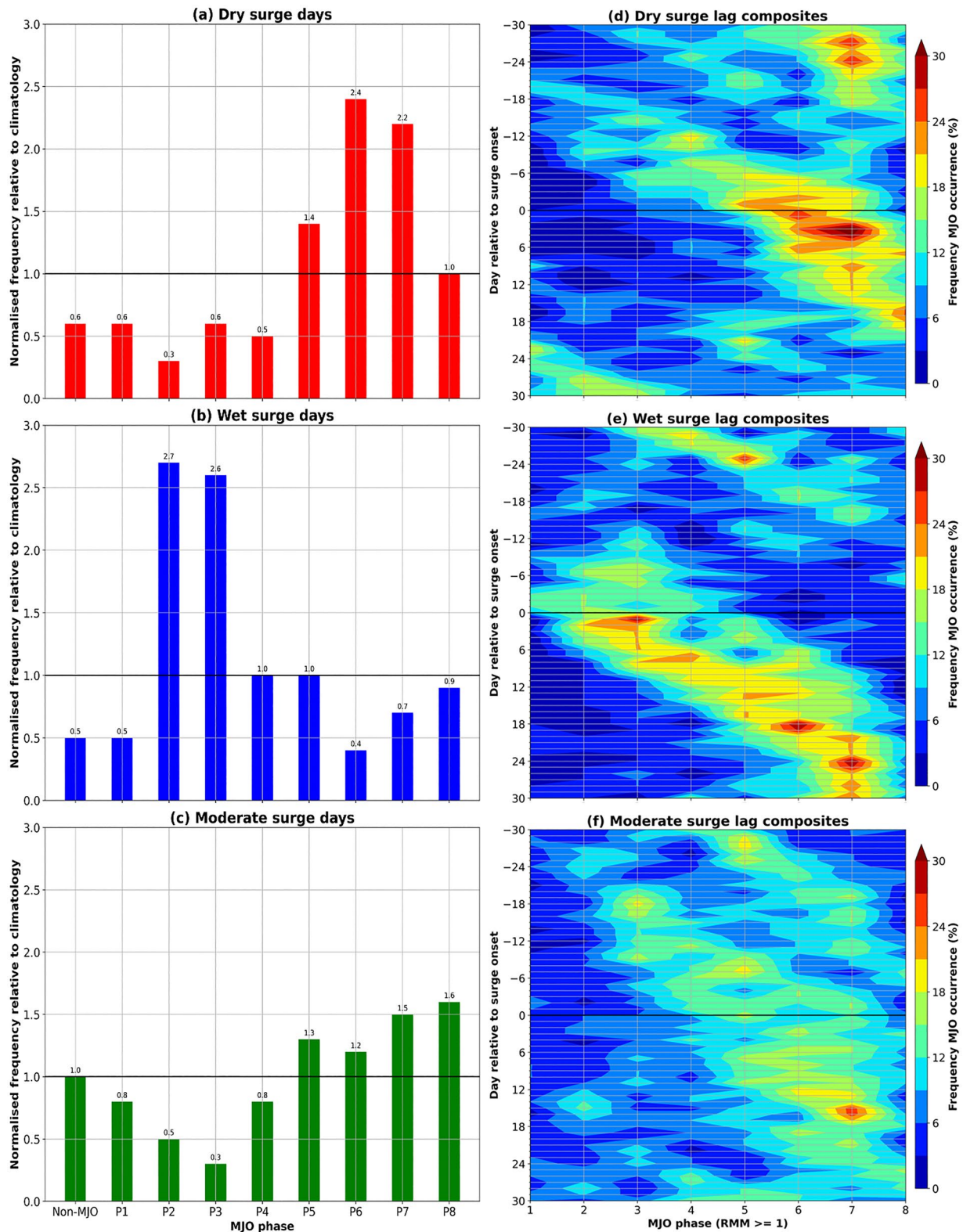


Figure 8. Left column: Normalized frequency for phases of the Madden-Julian Oscillation (MJO) (including non-MJO days where $RMM < 1$) relative to climatology where the amplitude is greater than or equal to 1. The horizontal black line is drawn at a normalized frequency of 1.0, where the percentage occurrence of a particular phase of the MJO is equal to that of the climatology. Right column: Lagged composite plots showing the percentage frequency of occurrence in a given phase of the MJO for each day from day -30 to day $+30$ relative to surge onset. (a, d) Dry, (b, e) wet, and (c, f) moderate cold surges. A non-MJO day is defined where $RMM < 1$.

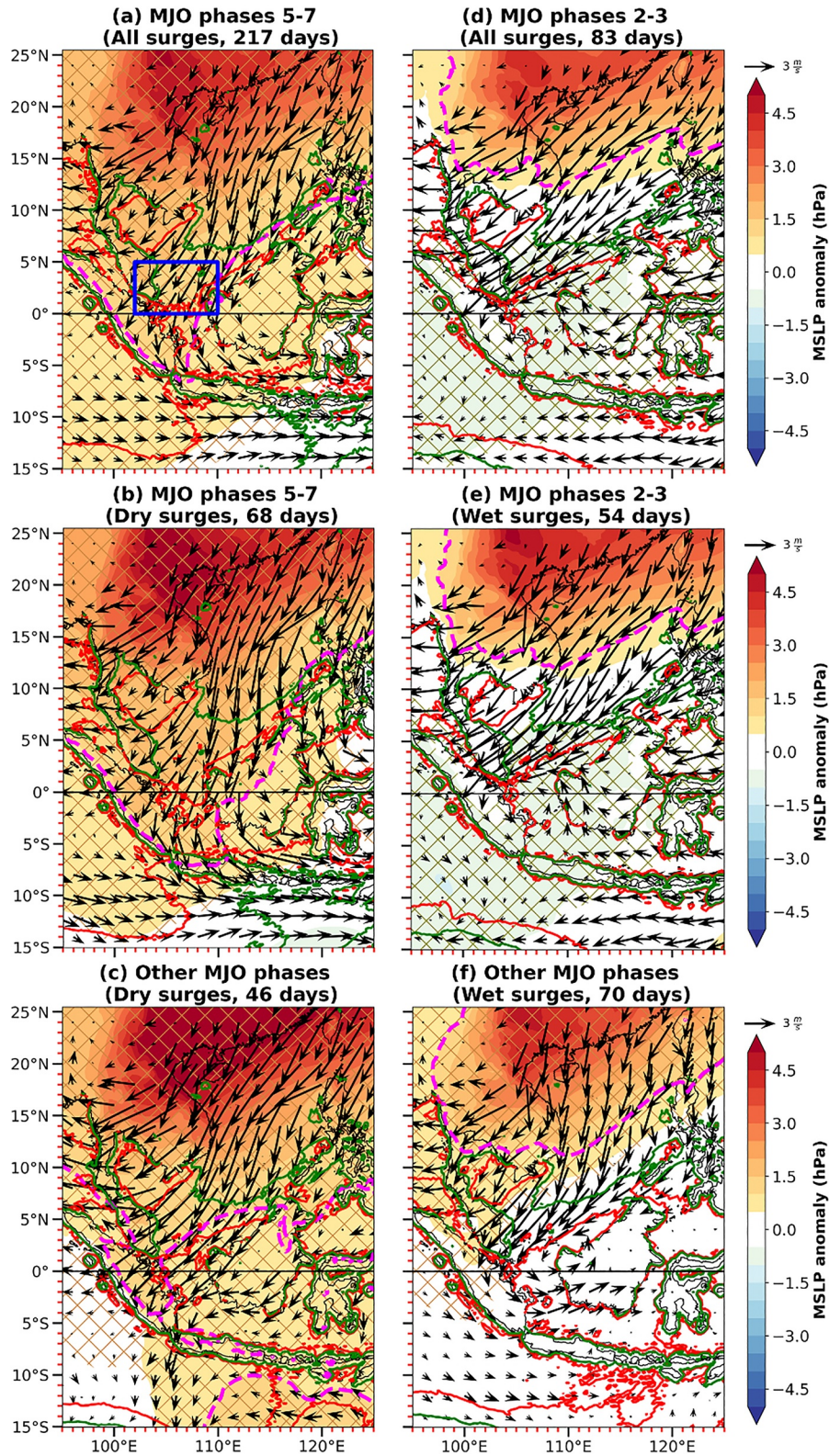


Figure 9.

(Figures 9d–9f). In both the active MJO phases and wet composites, the $0.15 \text{ hPa deg}^{-1}$ horizontal gradient contour approximately denotes the leading edge of the surge.

The synoptic environment in which dry or wet surges form is closely related to the MJO phase, and we note that the category of cold surge depends solely on the daily mean rainfall over the precipitation domain. Cold surges that form in phases 5–7 (phases 2–3) of the MJO have almost identical large-scale composite means, even if the surges are not categorized as dry (wet). According to the normalized frequencies in Figure 8, most of these other surges would fall into the moderate category. The pattern for dry surges outside phases 5–7 of the MJO is very similar in the Northern Hemisphere but different to the south of the equator, which suggests that the surge only crosses the equator and turns to westerly in the suppressed phases. The pattern for wet surges outside phases 2–3 of the MJO are different close to the equator and into the Southern Hemisphere where low-pressure anomalies are absent, and there are weak westerly anomalies over Java. In contrast to the cross-equatorial flow and westerlies in the suppressed phases, there are easterlies over Java and limited cross-equatorial flow in the active phases. Finally, the TCWV anomalies on day +1 in Figures 4b and 4d, which are consistent with the MSLP anomaly patterns, also suggest that the flow crosses the equator when the environment is dry, but is opposed in moist conditions.

6. Connections to the Australian Summer Monsoon

We now analyze the MSLP and GPM precipitation anomalies over the Australian monsoon domain, and statistical significance is shown for both under the 5th and above the 95th percentiles (Figure 10; see the green box in Figure 1). Like Figure 9, similar structures in the MSLP, precipitation, and 925 hPa horizontal wind anomalies are found when comparing the active and suppressed phases of the MJO for (a) all surges and (b) the wet and dry categories (Figures 10a, 10b, 10d, 10e, 10g, 10h, 10j, and 10k). According to Wheeler and Hendon (2004), phases 5–7 (phases 2–3) are the active (suppressed) phases of the MJO over the northern Australian region. Outside of the active and suppressed phases (Figures 10c, 10f, 10i, and 10l), cold surges with strong tropical cyclones over northern Australia that result in strong MSLP gradients are excluded due to their strong influence on the overall composites.

Westerly anomalies in phases 5–7 of the MJO and for the dry surge composites are associated with a significant north-west to south-east pressure gradient between Java and northern Australia (Figures 10a and 10b). The low-pressure anomalies peak at just under -1.0 hPa near the north-west coast of northern Australia, which is probably associated with tropical cyclones and monsoon lows. In contrast, the composites in phases 2–3 of the MJO and for wet surges depict a strong reversed pressure gradient associated with easterly anomalies, and with widespread high-pressure anomalies exceeding $+1.0 \text{ hPa}$ over much of northern Australia (Figures 10d and 10e). Outside these dominant phases, there are widespread and statistically significant high-pressure anomalies in the dry surge composites exceeding $+1.0 \text{ hPa}$ over most of the domain associated with weak easterly anomalies (Figure 10c). On the other hand, low-pressure anomalies (-0.1 to -0.9 hPa) and relatively weak westerly anomalies are found over most of northern Australia in the wet surge composites, and statistically significant low-pressure anomalies are confined to the south-eastern end of the domain (Figure 10f).

The GPM rainfall patterns also reflect the MJO patterns over the Australian monsoon domain. Statistically significant precipitation anomalies (exceeding $+10 \text{ mm d}^{-1}$ in some areas) are most widespread in the active phases of the MJO and for the dry surge composites (Figures 10g and 10h). Dry anomalies (-1 to -9 mm d^{-1}) are found over much of northern Australia in the suppressed phases and for the wet surge composites, while the wet anomalies are confined to Java (Figures 10j and 10k). Outside the dominant phases, negative precipitation anomalies (peaking close to -10 mm d^{-1}) lie over much of northern Australia in the dry surge composites, with positive anomalies also confined to Java (Figure 10i). The precipitation structure here is similar to the composites in Figures 10j and 10k, although the dry anomalies are less statistically significant and the easterly anomalies are weaker. In contrast, patches of statistically significant wet anomalies are found outside the dominant phases of the wet surge composites (Figure 10l). The strongly enhanced precipitation anomalies here do not appear to be associated with convectively active phases in the Australian summer monsoon, unlike the dry surge composites

Figure 9. Composite maps of daily mean sea-level pressure (MSLP) anomalies with the seasonal cycle removed. Daily mean 925 hPa horizontal wind anomaly vectors. (a, d) Dominant phases of the Madden-Julian Oscillation for all cold surges, (b) dry and (e) wet surges. (c, f) All other phases including non-MJO days. The precipitation domain is depicted by the blue box. The dashed magenta line shows the $+1.0 \text{ hPa}$ anomaly contour. The solid red and green contours show the absolute MSLP horizontal gradient magnitude at approximately 0.15 and $0.30 \text{ hPa deg}^{-1}$, respectively. The orange (green) hatching depicts areas where the MSLP anomalies are above (under) the 95th (5th) percentile for high (low) pressure anomalies.

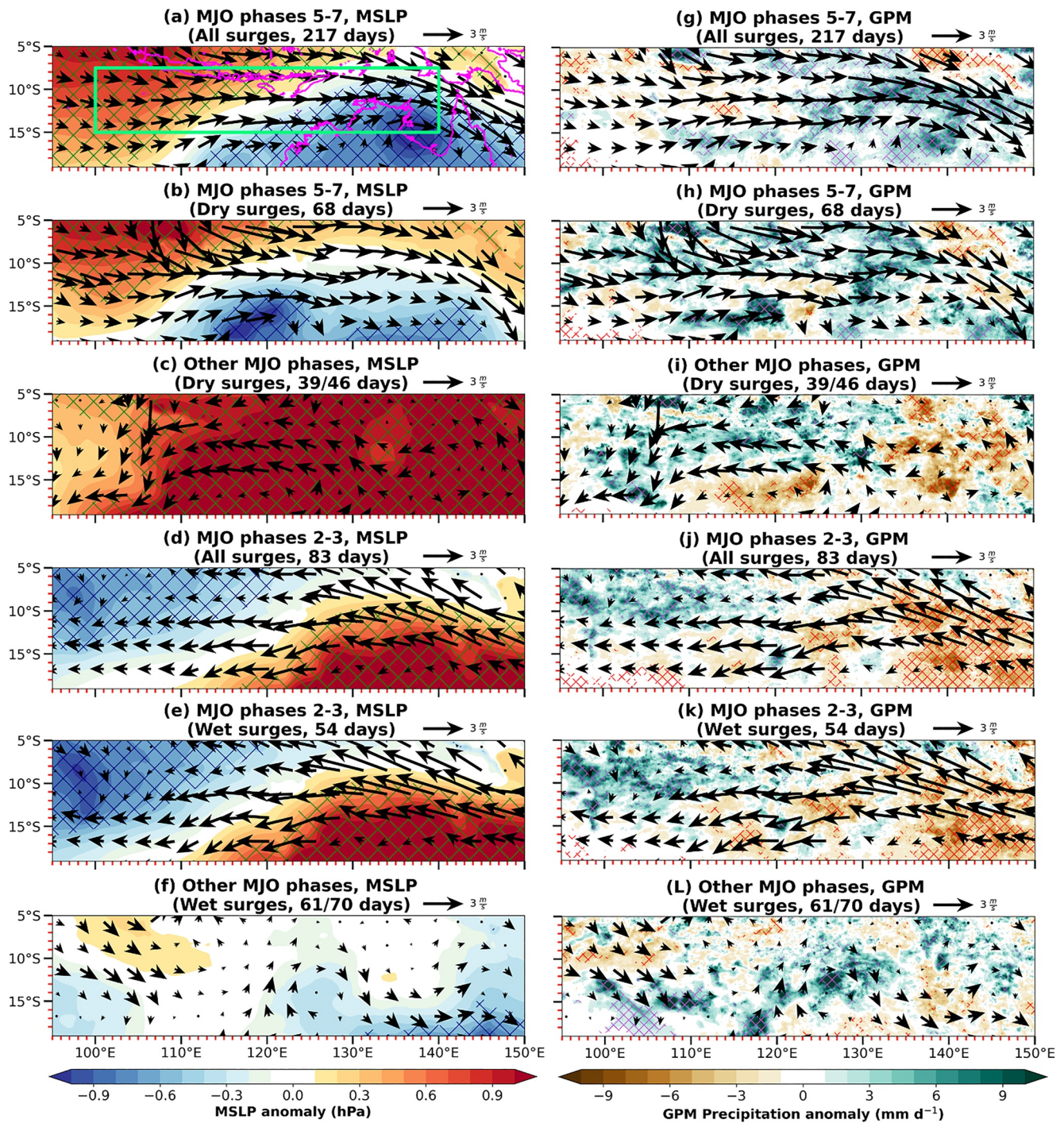


Figure 10. Composite maps of daily mean mean sea-level pressure (MSLP) anomalies (left column) and daily mean Global Precipitation Measurement precipitation anomalies (right column) with the seasonal cycle removed. Daily mean 925 hPa horizontal wind anomaly vectors. (a, d, g, j) Dominant phases of the Madden-Julian Oscillation for all cold surges, (b, h) dry, and (e, k) wet surges. (c, f, i, l) All other phases including non-MJO days. The Australian monsoon domain is depicted by the green box, and pink contours denote coastlines. Cold surges that coincide with strong tropical cyclones over northern Australia outside the dominant phases are removed. The green (navy) stippling depicts areas where MSLP anomalies are above (under) the 95th (5th) percentile for high (low) pressure anomalies. The red (navy) hatching depicts areas where precipitation anomalies are under (above) the 5th (95th) percentile.

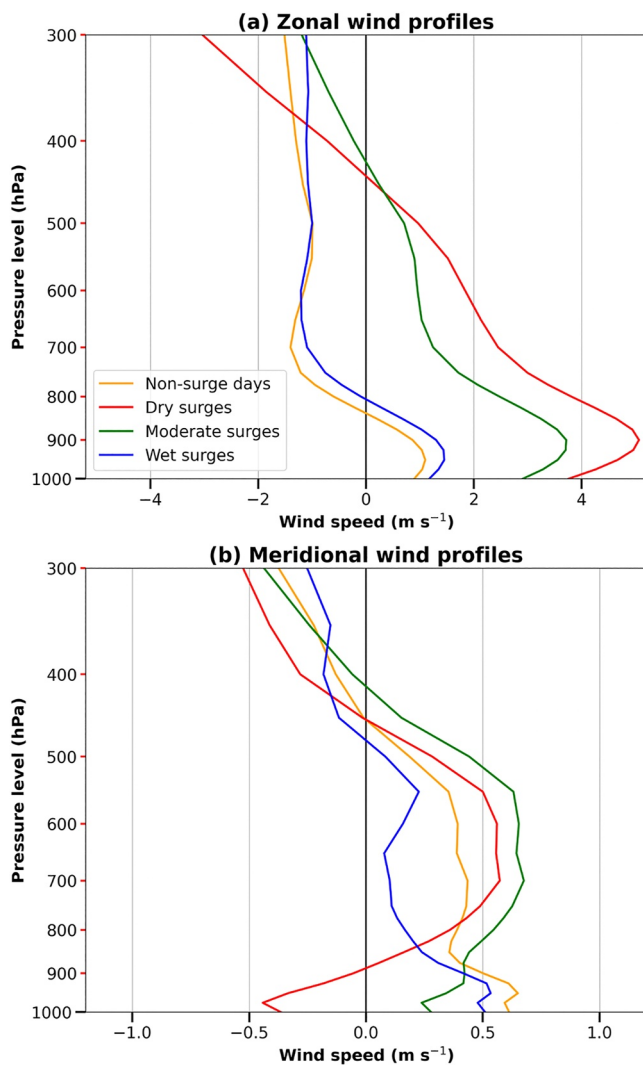


Figure 11. Vertical profiles of (a) zonal and (b) meridional winds from 1,000 to 300 hPa averaged over the Australian monsoon domain. Non-surge days (orange), and dry (red), moderate (green), and wet (blue) cold surges.

in phases 5–7 of the MJO, since there are a lack of both cross-equatorial flow and westerly anomalies over the region (see also Figure 9f).

From vertical profiles of the zonal winds (Figure 11a), the westerlies peak around 900 hPa in all cases, but are strongest (close to 5 m s^{-1}) in the dry surge composites and weakest in the non-surge composites. In the dry and moderate composites, the westerlies extend to approximately 450 hPa, which is close to the “deep westerly regime” profile in Pope et al. (2009), who investigated the regimes of the wet season in northern Australia. In their study, westerlies reach 350 hPa before transitioning to easterlies. On the other hand, the wet surge and non-surge composites depict only shallow westerlies, from the surface to approximately 800 hPa, and their zonal wind profiles are similar. The meridional winds (Figure 11b) are generally weak ($<1 \text{ m s}^{-1}$) in all composites throughout most of the troposphere, although northerly winds (peaking close to -0.5 m s^{-1}) are found from 1,000 to 900 hPa in the dry surge composites, which are likely a result of cross-equatorial flow from cold surges.

Our results suggest a clear relationship between the cold surge category, the MJO, and the westerlies over northern Australia that are sometimes associated with convectively active phases in the summer monsoon. These results are also consistent with most dry (wet) surges coinciding with phases 5–7 (phases 2–3) of the MJO. The strong link to the background MJO on the regional scale also explains why the majority of cases within the dry surge composites would be associated with westerlies and convectively active phases in the summer monsoon, and vice versa in the wet surge composites. According to Narsey et al. (2017), about one-third of the bursts in the Australian summer monsoon are associated with the MJO, whereas the more important influence on monsoon bursts is the equatorward extension of midlatitude weather systems. However, our study only addresses those monsoon bursts associated with the MJO.

7. Conclusions

In this study, we have reported the synoptic structure and development of dry, moderate, and wet cold surges over the Maritime Continent region over 20 November–March seasons. The category of cold surge solely depends on the daily mean rainfall over the precipitation domain. The study has included an investigation of both the seasonal and diurnal cycles, where the seasonal

cycle has been removed for all anomaly calculations. We have also examined the relationship between the MJO and cold surges and the Australian summer monsoon.

The plume buoyancy (B_L), introduced by Adames et al. (2021), was used to identify the local environmental differences responsible for the differences in the convection, and hence rainfall in the three categories. Following Adames et al. (2021), the precipitation increases exponentially as B_L increases toward zero. For most wet surge days, B_L exceeds -0.02 m s^{-2} , which is the boundary between a linear and exponential increase in precipitation according to Adames et al. (2021). Most dry surge days do not exceed the threshold. The diurnal cycle of B_L is also consistent with that of the GPM precipitation anomalies. These results suggest that the convective onset, and hence the diurnal precipitation patterns, are controlled by B_L . Moreover, the wet surges in particular are characterized by a moister free troposphere than non-surge days over the South China Sea because this reduces the effect of entrainment and allows convection to penetrate deeper.

On the synoptic scale, cold surges over the northern South China Sea are characterized by positive MSLP and negative TCWV anomalies, and enhanced descent or weaker ascent as the 700 hPa ω anomalies are negative. In all cases, the surge winds are almost entirely ageostrophic. For the dry surge composites, these characteristics are also found over the precipitation domain, with enhanced ascent and moist air over Java. Additionally, in close to

half the precipitation domain the absolute TCWV falls below the 48 mm threshold, marking a well-defined moist regime in the tropics as defined by Mapes et al. (2018). In the wet surge composites, the +1.0 hPa contour is confined to north of 10°N, and there is strongly enhanced ascent and low-pressure anomalies over the equatorial South China Sea. There is also a meridional TCWV anomaly gradient that is characterized by dry anomalies over the northern South China Sea and moist anomalies over the equator. A moist synoptic environment is already present over most parts of the South China Sea in the days prior to the wet surge onset. In contrast, dry anomalies spread from the Philippines and its surroundings and strengthen over the South China Sea in the days prior to the dry surge onset, merging with the stronger dry surge anomalies by the onset. The cyclonic circulation anomaly near Borneo, particularly evident in the difference between the wet and dry composites, coincides with upward motion. The wind field associated with this vortex opposes the surge north-easterlies and hence any cross-equatorial flow. The vortex also produces a strengthening of surge winds over the Malaysian Peninsula and a weakening over Borneo in the wet surges.

The development and southward propagation of the surge is qualitatively consistent with geostrophic adjustment on the beta plane as first described by H. Lim and Chang (1981). We find that the north-easterly wind anomalies propagate rapidly along the South China Sea equatorward (consistent with the propagation of a wave), whereas the negative anomalies of θ_e at 925 hPa (i.e., colder and drier air) spread more slowly as consistent with advection. In the vertical, descent with cold and dry anomalies deepen and strengthen between day -1 and day $+1$, and are strongest and most widespread in the dry surge composites. Warm and moist anomalies are most widespread near the equator on day $+1$ in the wet surge composites. The corresponding precipitation anomalies just to the north of the equator peak at approximately $+50 \text{ mm d}^{-1}$. The wet surge composites are also associated with stronger north-easterly winds and ascent between approximately 5°N and 12°N, and weaker north-easterly winds just to the north of the equator compared to the dry composites, which is consistent with limited cross-equatorial flow.

The regional-scale effects on the development of wet and dry surges has also been investigated. We find that the circulation patterns of wet (dry) surges are characteristic of the “South China Sea type” (“Both type”) surges in Abdillah et al. (2021). The synoptic environment in which wet or dry surges form is closely related to the MJO phase. There is a higher frequency of active (suppressed) phases (phases 5–7 and 2–3 respectively) of the MJO associated with the onset of wet (moderate and dry) surges. Dry and moderate surges occur predominantly in the suppressed phases as part of the eastward propagation of the MJO convective envelope, while wet surges sometimes appear to trigger the MJO, and often signal the start of the eastward propagation of the MJO. Cold surges that form in the suppressed (active) phases have almost identical large-scale composite means, even if the surges are not categorized as dry (wet). Outside these phases, the patterns differ particularly to the south of the equator, which suggests that only in the suppressed (active) phases are cold surges characterized by cross-equatorial flow and westerlies (limited cross-equatorial flow and easterlies) over Java.

Westerly anomalies in the dry surge composites and phases 5–7 of the MJO coincide with high-pressure anomalies over Java while low-pressure anomalies lie over northern Australia. This low-pressure anomaly is generally accompanied by westerly anomalies and increased precipitation, which together can be interpreted as a more active Australian monsoon. Nonetheless, this burst in the monsoon should not be attributed solely to the dry surge as it is inextricably tied to the MJO. The lack of cross-equatorial flow and westerlies outside phases 5–7 of the MJO coincide with widespread high-pressure anomalies extending to Java and northern Australia. In phases 2–3 of the MJO and the wet surge composites, low-pressure anomalies are found over Java while strong high-pressure anomalies are found over northern Australia. This configuration leads to a relatively inactive phase (commonly called a break) in the Australian monsoon.

Data Availability Statement

All data used in this manuscript are publicly available. The ERA5 datasets are publicly available at <https://cds.climate.copernicus.eu/cdsapp#!/dataset/reanalysis-era5-single-levels?tab=overview> (Hersbach et al., 2023) (single levels) and <https://cds.climate.copernicus.eu/cdsapp#!/dataset/reanalysis-era5-pressure-levels?tab=overview> (pressure levels). The National Computational Infrastructure (NCI) supercomputer (NCI, 2021; <https://nci.org.au/>) was remotely accessed to analyze the ERA5 datasets from the rt52 workspace. The GPM data may be obtained from <https://doi.org/10.5067/GPM/IMERGDF/DAY/06> for daily data (Huffman et al., 2019a) and <https://doi.org/10.5067/GPM/IMERG/3B-HH/06> for half-hourly data (Huffman et al., 2019b). Daily MJO data are available from the Australian Bureau of Meteorology (2023) at <http://www.bom.gov.au/climate/mjo/>.

Acknowledgments

We would like to acknowledge the suggestions and comments from the two reviewers as their insights significantly improved the paper. Tan was funded by the Monash International Tuition Scholarship (MITS) and the Maxwell King PhD Scholarship. Reeder was funded by the Australian Research Council, Centre of Excellence for Climate Extremes (CE170100023). Birch and Peatman were funded by the Natural Environmental Research Council (NERC) large grant, TerraMaris (NE/R016739/1). Birch was also funded by the Systematic Analysis of Real Time Forecasts (FORSEA) project, funded by the Met Office Weather and Climate Science for Service Partnership (WCSSP) Southeast Asia, as part of the Newton Fund. We are grateful for the use of the National Computational Infrastructure (NCI) facilities to analyze ERA5 data that was originally downloaded from the Copernicus Climate Change Service (C3S) Climate Data Store, GPM-IMERG data from Goddard Earth Sciences Data and Information Services Centre and the Wheeler-Hendon MJO index from the Australian Bureau of Meteorology.

References

- Abdillah, M. R., Kanno, Y., Iwasaki, T., & Matsumoto, J. (2021). Cold surge pathways in East Asia and their tropical impacts. *Journal of Climate*, 34(1), 157–170. <https://doi.org/10.1175/jcli-d-20-0552.1>
- Adames, Á. F., Powell, S. W., Ahmed, F., Mayta, V. C., & Neelin, J. D. (2021). Tropical precipitation evolution in a buoyancy-budget framework. *Journal of the Atmospheric Sciences*, 78(2), 509–528. <https://doi.org/10.1175/JAS-D-20-0074.1>
- Ahmed, F., & Neelin, J. D. (2018). Reverse engineering the tropical precipitation–buoyancy relationship. *Journal of the Atmospheric Sciences*, 75(5), 1587–1608. <https://doi.org/10.1175/jas-d-17-0333.1>
- Ambaum, M. H. P. (2010). Significance tests in climate science. *Journal of Climate*, 23(22), 5927–5932. <https://doi.org/10.1175/2010jcli3746.1>
- Argüeso, D., Romero, R., & Homar, V. (2020). Precipitation features of the Maritime continent in parameterized and explicit convection models. *Journal of Climate*, 33(6), 2449–2466. <https://doi.org/10.1175/JCLI-D-19-0416.1>
- Berry, G. J., & Reeder, M. J. (2016). The dynamics of Australian monsoon bursts. *Journal of the Atmospheric Sciences*, 73(1), 55–69. <https://doi.org/10.1175/JAS-D-15-0071.1>
- Bureau of Meteorology. (2023). Madden-Julian Oscillation (MJO) [Dataset]. Australian Government Bureau of Meteorology. Retrieved from <http://www.bom.gov.au/climate/mjo/>
- Chang, C.-P., Erickson, J. E., & Lau, K. M. (1979). Northeasterly cold surges and near-equatorial disturbances over the winter MONEX area during December 1974. Part I: Synoptic aspects. *Monthly Weather Review*, 107(7), 812–829. [https://doi.org/10.1175/1520-0493\(1979\)107<0812:NCSANE>2.0.CO;2](https://doi.org/10.1175/1520-0493(1979)107<0812:NCSANE>2.0.CO;2)
- Chang, C.-P., Harr, P. A., & Chen, H.-J. (2005). Synoptic disturbances over the equatorial South China Sea and Western Maritime continent during boreal winter. *Monthly Weather Review*, 133(3), 489–503. <https://doi.org/10.1175/MWR-2868.1>
- Chang, C.-P., Liu, C.-H., & Kuo, H.-C. (2003). Typhoon Vamei: An equatorial tropical cyclone formation. *Geophysical Research Letters*, 30(3), 1150. <https://doi.org/10.1029/2002GL016365>
- Chang, C.-P., Lu, M.-M., & Wang, S. (2004). The East Asian winter monsoon. In *The global monsoon system* (pp. 99–109).
- Chang, C.-P., Millard, J. E., & Chen, G. T. J. (1983). Gravitational character of cold surges during winter MONEX. *Monthly Weather Review*, 111(2), 293–307. [https://doi.org/10.1175/1520-0493\(1983\)111<0293:GCOCSND>2.0.CO;2](https://doi.org/10.1175/1520-0493(1983)111<0293:GCOCSND>2.0.CO;2)
- Cheang, B. K. (1977). Synoptic features and structures of some equatorial vortices over the South China Sea in the Malaysian region during the winter monsoon, December 1973. *Pure and Applied Geophysics*, 115(5), 1303–1333. <https://doi.org/10.1007/BF00874411>
- Davidson, N. E., McBride, J. L., & McAvaney, B. J. (1983). The onset of the Australian monsoon during winter MONEX: Synoptic aspects. *Monthly Weather Review*, 111(3), 496–516. [https://doi.org/10.1175/1520-0493\(1983\)111<0496:TOOTAM>2.0.CO;2](https://doi.org/10.1175/1520-0493(1983)111<0496:TOOTAM>2.0.CO;2)
- de Rooy, W. C., & Siebesma, A. P. (2010). Analytical expressions for entrainment and detrainment in cumulus convection. *Quarterly Journal of the Royal Meteorological Society*, 136(650), 1216–1227. <https://doi.org/10.1002/qj.640>
- Ding, Y. (1990). Build-up, air mass transformation and propagation of Siberian high and its relations to cold surge in East Asia. *Meteorology and Atmospheric Physics*, 44(1), 281–292. <https://doi.org/10.1007/BF01026822>
- Ding, Y. (1994). *Monsoons over China* (pp. 91–173). Kluwer Academic Publishers.
- Feng, J., Lian, T., Ding, Y., Li, X., Sun, C., & Chen, D. (2022). Two types of the east Asian cold surge and their impacts on El Niño. *Geophysical Research Letters*, 49(3), e2021GL096108. <https://doi.org/10.1029/2021GL096108>
- Fong, M., & Ng, L. K. (2012). *The weather and climate of Singapore* (pp. 70–97). Meteorological Service Singapore.
- Gill, J. (1999). The insignificance of Null hypothesis significance testing. *Political Research Quarterly*, 52(3), 647–674. <https://doi.org/10.1177/106591299905200309>
- Gregory, D. (2001). Estimation of entrainment rate in simple models of convective clouds. *Quarterly Journal of the Royal Meteorological Society*, 127(571), 53–72. <https://doi.org/10.1002/qj.49712757104>
- Hersbach, H., Bell, B., Berrisford, P., Biavati, G., Horányi, A., Muñoz-Sabater, J., et al. (2023). ERA5 hourly data on pressure levels from 1940 to present [Dataset]. Copernicus Climate Change Service (C3S) Climate Data Store (CDS). Retrieved from <https://cds.climate.copernicus.eu/cdsapp#!/dataset/reanalysis-era5-pressure-levels?tab=overview>
- Hersbach, H., Bell, B., Berrisford, P., Hirahara, S., Horányi, A., Muñoz-Sabater, J., et al. (2020). The ERA5 global reanalysis. *Quarterly Journal of the Royal Meteorological Society*, 146(730), 1999–2049. <https://doi.org/10.1002/qj.3803>
- Huffman, G. J., Bolvin, D. T., Braithwaite, D., Hsu, K., Joyce, R., Kidd, C., et al. (2019). *NASA global precipitation measurement (GPM) integrated multi-satellite retrievals for GPM (IMERG), algorithm theoretical basis document (ATBD) version 06*. National Aeronautics and Space Administration.
- Huffman, G. J., Stocker, E. F., Bolvin, D. T., Nelkin, E. J., & Tan, J. (2019a). GPM IMERG final precipitation L3 1 day 0.1 degree × 0.1 degree V06 [Dataset]. Goddard Earth Sciences Data and Information Services Centre (GES DISC). Retrieved from https://disc.gsfc.nasa.gov/datasets/GPM_3IMERGDF_06/summary
- Huffman, G. J., Stocker, E. F., Bolvin, D. T., Nelkin, E. J., & Tan, J. (2019b). GPM IMERG final precipitation L3 half hourly 0.1 degree × 0.1 degree V06 [Dataset]. Goddard Earth Sciences Data and Information Services Centre (GES DISC). Retrieved from https://disc.gsfc.nasa.gov/datasets/GPM_3IMERGHH_06/summary
- Johnson, D. H. (1999). The insignificance of statistical significance testing. *Journal of Wildlife Management*, 63(3), 763–772. <https://doi.org/10.2307/3802789>
- Johnson, R. H., & Chang, C.-P. (2007). Winter MONEX: A quarter-century and beyond. *Bulletin of the American Meteorological Society*, 88(3), 385–388. <https://doi.org/10.1175/BAMS-88-3-385>
- Johnson, R. H., & Houze, R. A., Jr. (1987). Precipitating cloud systems of the Asian monsoon. In *Monsoon Meteorology*. Retrieved from <https://ci.nii.ac.jp/naid/10014597164/en/>
- Johnson, R. H., & Zimmerman, J. R. (1986). Modification of the boundary layer over the South China sea during a winter MONEX cold surge event. *Monthly Weather Review*, 114(11), 2004–2015. [https://doi.org/10.1175/1520-0493\(1986\)114<2004:mothlo>2.0.co;2](https://doi.org/10.1175/1520-0493(1986)114<2004:mothlo>2.0.co;2)
- Koseki, S., Koh, T. Y., & Teo, C. K. (2014). Borneo vortex and mesoscale convective rainfall. *Atmospheric Chemistry and Physics*, 14(9), 4539–4562. <https://doi.org/10.5194/acp-14-4539-2014>
- Lau, K.-M., & Li, M.-T. (1984). The monsoon of East Asia and its global associations—A survey. *Bulletin of the American Meteorological Society*, 65(2), 114–125. [https://doi.org/10.1175/1520-0477\(1984\)065<0114:TMOEAA>2.0.CO;2](https://doi.org/10.1175/1520-0477(1984)065<0114:TMOEAA>2.0.CO;2)
- Lim, H., & Chang, C.-P. (1981). A theory for midlatitude forcing of tropical motions during winter monsoons. *Journal of the Atmospheric Sciences*, 38(11), 2377–2392. [https://doi.org/10.1175/1520-0469\(1981\)038<2377:ATFMFO>2.0.CO;2](https://doi.org/10.1175/1520-0469(1981)038<2377:ATFMFO>2.0.CO;2)
- Lim, S. Y., Marzin, C., Xavier, P., Chang, C.-P., & Timbal, B. (2017). Impacts of boreal winter monsoon cold surges and the interaction with MJO on Southeast Asia rainfall. *Journal of Climate*, 30(11), 4267–4281. <https://doi.org/10.1175/JCLI-D-16-0546.1>

- Love, G. (1985). Cross-equatorial influence of winter Hemisphere subtropical cold surges. *Monthly Weather Review*, *113*(9), 1487–1498. [https://doi.org/10.1175/1520-0493\(1985\)113<1487:CEIOWH>2.0.CO;2](https://doi.org/10.1175/1520-0493(1985)113<1487:CEIOWH>2.0.CO;2)
- Mapes, B. E., Chung, E. S., Hannah, W. M., Masunaga, H., Wimmers, A. J., & Velden, C. S. (2018). The meandering margin of the meteorological moist tropics. *Geophysical Research Letters*, *45*(2), 1177–1184. <https://doi.org/10.1002/2017GL076440>
- McBride, J. L., Sahany, S., Hassim, M. E. E., Nguyen, C. M., Lim, S.-Y., Rahmat, R., & Cheong, W.-K. (2015). The 2014 record dry spell at Singapore: An intertropical convergence Zone (ITCZ) drought. *Bulletin of the American Meteorological Society*, *96*(12), S126–S130. <https://doi.org/10.1175/bams-d-15-00117.1>
- Meteorological Service Singapore (MSS). (2022a). 2021 annual climate assessment Singapore. Retrieved from <http://www.weather.gov.sg/climate-annual-climate-reports/>
- Meteorological Service Singapore (MSS). (2022b). Weather systems. Retrieved from http://www.weather.gov.sg/learn_weather_systems/
- Narsey, S., Reeder, M. J., Ackerley, D., & Jakob, C. (2017). A midlatitude influence on Australian monsoon bursts. *Journal of Climate*, *30*(14), 5377–5393. <https://doi.org/10.1175/JCLI-D-16-0686.1>
- Narsey, S., Reeder, M. J., Jakob, C., & Ackerley, D. (2018). An evaluation of northern Australian wet season rainfall bursts in CMIP5 models. *Journal of Climate*, *31*(19), 7789–7802. <https://doi.org/10.1175/JCLI-D-17-0637.1>
- NCI. (2021). NCI Australia [ComputationalInfrastructure]. Retrieved from <https://nci.org.au/>
- Neale, R., & Slingo, J. (2003). The Maritime continent and its role in the global climate: A GCM study. *Journal of Climate*, *16*(5), 834–848. [https://doi.org/10.1175/1520-0442\(2003\)016<0834:TMCAIR>2.0.CO;2](https://doi.org/10.1175/1520-0442(2003)016<0834:TMCAIR>2.0.CO;2)
- Nicholls, N. (2001). The insignificance of significance testing. *Bulletin of the American Meteorological Society*, *82*(5), 981–986. [https://doi.org/10.1175/1520-0477\(2001\)082<0981:caatio>2.3.co;2](https://doi.org/10.1175/1520-0477(2001)082<0981:caatio>2.3.co;2)
- Pope, M., Jakob, C., & Reeder, M. J. (2009). Regimes of the north Australian wet season. *Journal of Climate*, *22*(24), 6699–6715. <https://doi.org/10.1175/2009jcli3057.1>
- Pullen, J., Gordon, A. L., Flatau, M., Doyle, J. D., Villanoy, C., & Cabrera, O. (2015). Multiscale influences on extreme winter rainfall in the Philippines. *Journal of Geophysical Research: Atmospheres*, *120*(8), 3292–3309. <https://doi.org/10.1002/2014JD022645>
- Ramage, C. S. (1968). Role of a tropical “Maritime continent” in the atmospheric circulation. *Monthly Weather Review*, *96*(6), 365–370. [https://doi.org/10.1175/1520-0493\(1968\)096<0365:ROATMC>2.0.CO;2](https://doi.org/10.1175/1520-0493(1968)096<0365:ROATMC>2.0.CO;2)
- Ramage, C. S. (1971). *Monsoon Meteorology* (pp. 229–242). Academic Press.
- Raymond, D., Fuchs, Ž., Gjorgjievska, S., & Sessions, S. (2015). Balanced dynamics and convection in the tropical troposphere. *Journal of Advances in Modeling Earth Systems*, *7*(3), 1093–1116. <https://doi.org/10.1002/2015MS000467>
- Suppiah, R., & Wu, X. (1998). Surges, cross-equatorial flows and their links with the Australian summer monsoon circulation and rainfall. *Australian Meteorological Magazine*, *47*(2), 113–130.
- Tangang, F. T., Juneng, L., Salimun, E., Vinayachandran, P. N., Seng, Y. K., Reason, C. J. C., et al. (2008). On the roles of the northeast cold surge, the Borneo vortex, the Madden-Julian Oscillation, and the Indian Ocean Dipole during the extreme 2006/2007 flood in southern Peninsular Malaysia. *Geophysical Research Letters*, *35*(14), L14S07. <https://doi.org/10.1029/2008GL033429>
- Warner, C. (1982). Mesoscale features and cloud Organization on 10–12 December 1978 over the South China sea. *Journal of the Atmospheric Sciences*, *39*(7), 1619–1641. [https://doi.org/10.1175/1520-0469\(1982\)039<1619:MFACOO>2.0.CO;2](https://doi.org/10.1175/1520-0469(1982)039<1619:MFACOO>2.0.CO;2)
- Wheeler, M. C., & Hendon, H. H. (2004). An all-season real-time multivariate MJO index: Development of an index for monitoring and prediction. *Monthly Weather Review*, *132*(8), 1917–1932. <https://doi.org/10.1175/1520-0493%282004%29132%3C1917%3AAARMMI%3E2.0.CO%3B2>
- Wu, P., Hara, M., Fudeyasu, H., Yamanaka, M. D., Matsumoto, J., Syamsudin, F., et al. (2007). The impact of trans-equatorial monsoon flow on the formation of repeated torrential rains over Java island. *SOLA*, *3*, 93–96. <https://doi.org/10.2151/sola.2007-024>
- Xavier, P., Lim, S. Y., Ammar Bin Abdullah, M. F., Bala, M., Chenoli, S. N., Handayani, A. S., et al. (2020). Seasonal dependence of cold surges and their interaction with the Madden–Julian Oscillation over Southeast Asia. *Journal of Climate*, *33*(6), 2467–2482. <https://doi.org/10.1175/JCLI-D-19-0048.1>
- Yang, J. H., Qian, J. H., & Timbal, B. (2019). A moisture flux perspective on cold surges and wet spells affecting Singapore. *MSS Research Letters*, *3*, 3–9. Retrieved from http://ccrs.weather.gov.sg/wp-content/uploads/2019/07/MRL_Issue_3_Jul2019_FINAL.pdf